

Solving Inverse Problems with Latent Diffusion Models via Hard Data Consistency

Bowen Song^{1*}, Soo Min Kwon^{1*}, Zecheng Zhang², Xinyu Hu³, Qing Qu¹, and Liyue Shen¹

¹Department of EECS, University of Michigan

²Kumo.AI

³Microsoft

Diffusion models have recently emerged as powerful generative priors for solving inverse problems. However, training diffusion models in the pixel space are both data-intensive and computationally demanding, which restricts their applicability as priors for high-dimensional real-world data such as medical images. Latent diffusion models, which operate in a much lower-dimensional space, offer a solution to these challenges. However, incorporating latent diffusion models to solve inverse problems remains a challenging problem due to the nonlinearity of the encoder and decoder. To address these issues, we propose *ReSample*, an algorithm that can solve general inverse problems with pre-trained latent diffusion models. Our algorithm incorporates data consistency by solving an optimization problem during the reverse sampling process, a concept that we term as hard data consistency. Upon solving this optimization problem, we propose a novel resampling scheme to map the measurement-consistent sample back onto the noisy data manifold and theoretically demonstrate its benefits. Lastly, we apply our algorithm to solve a wide range of linear and nonlinear inverse problems in both natural and medical images, demonstrating that our approach outperforms existing state-of-the-art approaches, including those based on pixel-space diffusion models.

1. Introduction

Inverse problems arise from a wide range of applications across many domains, including computational imaging [1, 2], medical imaging [3, 4], and remote sensing [5, 6], to name a few. When solving these inverse problems, the goal is to reconstruct an unknown signal $x_* \in \mathbb{R}^n$ given observed measurements $y \in \mathbb{R}^m$ of the form

$$y = \mathcal{A}(x_*) + \eta,$$

where $\mathcal{A}(\cdot) : \mathbb{R}^n \rightarrow \mathbb{R}^m$ denotes some forward measurement operator (can be linear or nonlinear) and $\eta \in \mathbb{R}^m$ is additive noise. Usually, we are interested in the case when $m < n$, which follows many real-world scenarios. When $m < n$, the problem is ill-posed and some kind of regularizer (or prior) is necessary to obtain a meaningful solution.

In the literature, the traditional approach of using hand-crafted priors (e.g. sparsity) is slowly being replaced by rich, learned priors such as deep generative models. Recently, there has been a lot of interests in using diffusion models as structural priors due to their state-of-the-art performance in image generation [7–9]. Compared to GANs, diffusion models are generally easier and more stable to train as they do not rely on an adversarial training scheme, making them a generative prior that is more readily accessible [7]. The most common approach for using diffusion models as

*Corresponding authors {bowenbw, kwonsm}@umich.edu

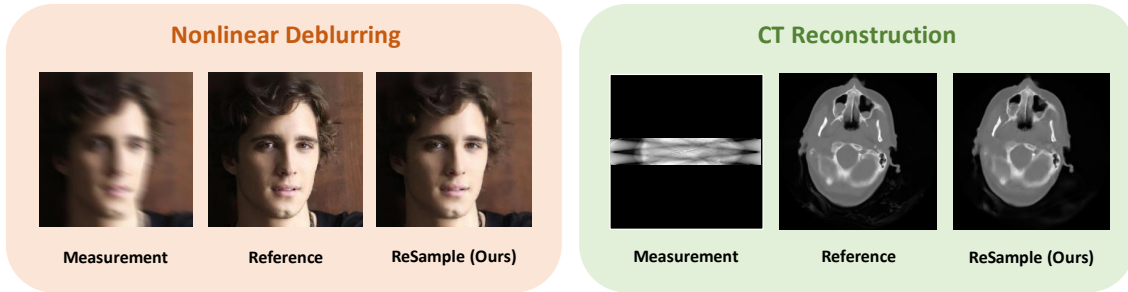


Figure 1: Example reconstructions of our algorithm (*ReSample*) on two noisy inverse problems, nonlinear deblurring and CT reconstruction, on natural and medical images, respectively.

priors is to resort to posterior sampling, which has been extensively explored in the literature [10–17]. However, despite their remarkable success, these techniques exhibit several limitations. The primary challenge is that the majority of existing works that employ diffusion models as priors train these models directly in the pixel space, which requires substantial computational resources and a large volume of training data. In real-world applications such as computed tomography (CT) and magnetic resonance imaging (MRI) reconstruction, where images are inherently either 3D or even 4D [18], training diffusion models directly in the pixel space is often infeasible.

Latent diffusion models (LDMs), which embed data in order to operate in a lower-dimensional space, present a potential solution to this challenge, along with considerable improvements in computational efficiency [19, 20]. They also can provide a great amount of flexibility, as they can enable one to transfer and generalize these models to different domains by fine-tuning on small amounts of training data. Nevertheless, how to use LDMs to solve inverse problems is a very challenging task. The main challenge comes from the fact that the encoder and decoder are very complicated neural networks. Due to the nonlinearity and the non-convexity of the decoder, one cannot simply adapt existing solvers that operate in the pixel space, as they are mostly formulated for linear inverse problems. Some concurrent work proposes an interesting method to solve inverse problems with LDMs [21]. More generally, our algorithm is not limited to linear inverse problems but, to our best knowledge, is the first that can deal with general inverse problems with LDMs.

In this work, we introduce a novel algorithm named *ReSample*, which effectively employs LDMs as priors for solving inverse problems. Our algorithm can be viewed as a two-stage process that incorporates data consistency by (1) solving a hard-constrained optimization problem, ensuring we obtain the correct latent variable that is consistent with the observed measurements, and (2) employing a carefully designed resampling scheme to map the measurement-consistent sample back onto the correct noisy data manifold. As a result, we show that our algorithm can achieve state-of-the-art performance on various inverse problem tasks and different datasets, compared to existing algorithms. Notably, owing to using the latent diffusion models as generative priors, our algorithm achieves improved computational efficiency with a reduction in memory complexity. Below, we highlight some of our key contributions.

- We propose a novel algorithm that enables us to leverage latent diffusion models for solving general inverse problems (linear and nonlinear) through hard data consistency.
- Particularly, we carefully design a stochastic resampling scheme that can reliably map the measurement-consistent samples back onto the noisy data manifold to continue the reverse sam-

pling process. We provide a theoretical analysis to further demonstrate the superiority of the proposed stochastic resampling technique.

- With extensive experiments on multiple tasks and various datasets, encompassing both natural and medical images, our proposed algorithm achieves state-of-the-art performance on a variety of linear and nonlinear inverse problems.

2. Background

2.1. Diffusion Models

Denoising Diffusion Probabilistic Models. We first briefly review the basic fundamentals of diffusion models, namely the denoising diffusion probabilistic model (DDPM) formulation [22]. Let $\mathbf{x}_0 \sim p_{\text{data}}(\mathbf{x})$ denote samples from the data distribution. Diffusion models start by progressively perturbing data to noise via Gaussian kernels, which can be written as the variance-preserving stochastic differential equation (VP-SDE) [23] of the form

$$d\mathbf{x} = -\frac{\beta_t}{2}\mathbf{x}dt + \sqrt{\beta_t}d\mathbf{w}, \quad (1)$$

where $\beta_t \in (0, 1)$ is the noise schedule that is a monotonically increasing sequence of t and \mathbf{w} is the standard Wiener process. This is generally defined such that we obtain the data distribution when $t = 0$ and obtain a Gaussian distribution when $t = T$, i.e. $\mathbf{x}_T \sim \mathcal{N}(\mathbf{0}, \mathbf{I})$. The objective of diffusion models is to learn the corresponding reverse SDE of Equation (1), which is of the form

$$d\mathbf{x} = \left[-\frac{\beta_t}{2}\mathbf{x} - \beta_t \nabla_{\mathbf{x}_t} \log p(\mathbf{x}_t) \right] dt + \sqrt{\beta_t}d\bar{\mathbf{w}}, \quad (2)$$

where $d\bar{\mathbf{w}}$ is the standard Wiener process running backward in time and $\nabla_{\mathbf{x}_t} \log p(\mathbf{x}_t)$ is the (Stein) score function. In practice, we approximate the score function using a neural network s_θ parameterized by θ , which can be trained via denoising score matching [24]:

$$\hat{\theta} = \arg \min_{\theta} \mathbb{E} [\|s_\theta(\mathbf{x}_t, t) - \nabla_{\mathbf{x}_t} \log p(\mathbf{x}_t|\mathbf{x}_0)\|_2^2], \quad (3)$$

where t is uniformly sampled from $[0, T]$ and the expectation is taken over t , $\mathbf{x}_t \sim p(\mathbf{x}_t|\mathbf{x}_0)$, and $\mathbf{x}_0 \sim p_{\text{data}}(\mathbf{x})$. Once we have access to the parameterized score function s_θ , we can use it to approximate the reverse-time SDE and simulate it using numerical solvers (e.g. Euler-Maruyama).

Denoising Diffusion Implicit Models. As the DDPM formulation is known to have a slow sampling process, Song et al. [25] proposed denoising diffusion implicit models (DDIMs) that defines the diffusion process as a non-Markovian process to remedy this [9, 22, 25, 26]. This enables a faster sampling process with the sampling steps given by

$$\mathbf{x}_{t-1} = \sqrt{\bar{\alpha}_{t-1}}\hat{\mathbf{x}}_0(\mathbf{x}_t) + \sqrt{1 - \bar{\alpha}_{t-1} - \eta\delta_t^2}\mathbf{s}_\theta(\mathbf{x}_t, t) + \eta\delta_t\epsilon, \quad t = T, \dots, 0, \quad (4)$$

where $\alpha_t = 1 - \beta_t$, $\bar{\alpha}_t = \prod_{i=1}^t \alpha_i$, $\epsilon \sim \mathcal{N}(\mathbf{0}, \mathbf{I})$, η is the temperature parameter, δ_t controls the stochasticity of the update step, and $\hat{\mathbf{x}}_0(\mathbf{x}_t)$ denotes the predicted \mathbf{x}_0 from \mathbf{x}_t which takes the form

$$\hat{\mathbf{x}}_0(\mathbf{x}_t) = \frac{1}{\sqrt{\bar{\alpha}_t}}(\mathbf{x}_t + \sqrt{1 - \bar{\alpha}_t}\mathbf{s}_\theta(\mathbf{x}_t, t)), \quad (5)$$

which is an application of Tweedie’s formula. Here, s_θ is usually trained using the epsilon-matching score objective [25]. We use DDIM as the backbone of our algorithm and show how we can leverage these update steps for solving inverse problems.

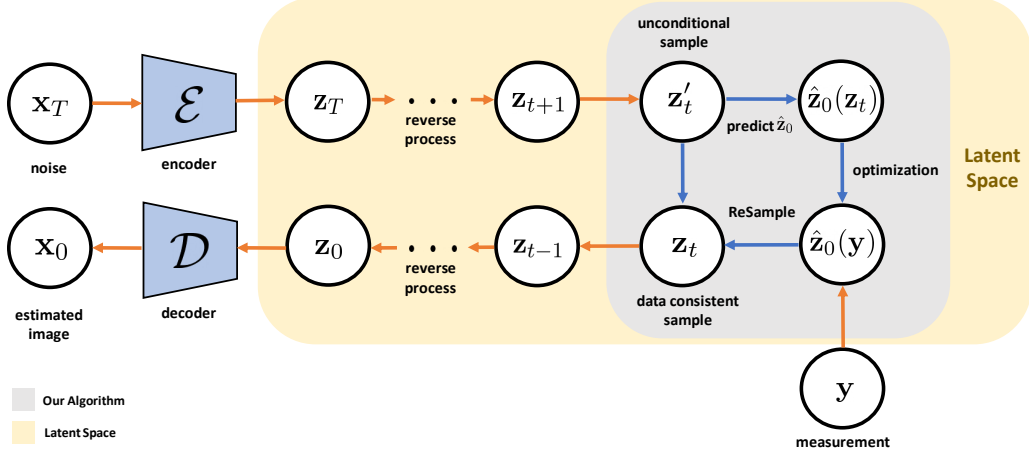


Figure 2: **Overview of our ReSample algorithm during the reverse sampling process conditioned on the data constraints from measurement.** The entire sampling process is conducted in the latent space upon passing the sample through the encoder. The proposed algorithm performs hard data consistency at some time steps t via a skipped-step mechanism.

2.2. Diffusion Models for Solving Inverse Problems

Solving Inverse Problems with Diffusion Models. Given measurements $\mathbf{y} \in \mathbb{R}^m$ from some forward measurement operator $\mathcal{A}(\cdot)$, we can use diffusion models to solve inverse problems by replacing the score function in Equation (2) with the conditional score function $\nabla_{\mathbf{x}_t} \log p(\mathbf{x}_t | \mathbf{y})$. Then by Bayes rule, notice that we can write the conditional score as

$$\nabla_{\mathbf{x}_t} \log p(\mathbf{x}_t | \mathbf{y}) = \nabla_{\mathbf{x}_t} \log p(\mathbf{x}_t) + \nabla_{\mathbf{x}_t} \log p(\mathbf{y} | \mathbf{x}_t).$$

This results in the reverse SDE of the form

$$d\mathbf{x} = \left[-\frac{\beta_t}{2} \mathbf{x} - \beta_t (\nabla_{\mathbf{x}_t} \log p(\mathbf{x}_t) + \nabla_{\mathbf{x}_t} \log p(\mathbf{y} | \mathbf{x}_t)) \right] dt + \sqrt{\beta_t} d\bar{\mathbf{w}}.$$

In the literature, solving this reverse SDE is referred as *posterior sampling*. However, the issue with posterior sampling is that there does not exist an analytical formulation for the likelihood term $\nabla_{\mathbf{x}_t} \log p(\mathbf{y} | \mathbf{x}_t)$. To resolve this, there exists two lines of work: (1) to resort to alternating projections onto the measurement subspace to avoid using the likelihood directly [12, 13, 27] and (2) to estimate the likelihood under some mild assumptions [11, 14]. For example, Chung et al. [11] proposed diffusion posterior sampling (DPS) that uses a Laplacian approximation of the likelihood, which results in the discrete update steps

$$\mathbf{x}_{t-1} = \sqrt{\bar{\alpha}_{t-1}} \hat{\mathbf{x}}_0(\mathbf{x}_t) + \sqrt{1 - \bar{\alpha}_{t-1} - \eta \delta_t^2} \mathbf{s}_\theta(\mathbf{x}_t, t) + \eta \delta_t \epsilon \quad (6)$$

$$\mathbf{x}_{t-1} = \mathbf{x}'_{t-1} - \zeta \nabla_{\mathbf{x}_t} \|\mathbf{y} - \mathcal{A}(\hat{\mathbf{x}}_0(\mathbf{x}_t))\|_2^2, \quad (7)$$

where $\zeta \in \mathbb{R}$ can be viewed as a tunable step-size. However, as previously mentioned, these techniques have limited applicability for real-world problems as they are all built on the pixel space.

Solving Inverse Problems with Latent Diffusion Models. The limited applicability of pixel-based diffusion models can be tackled by alternatively utilizing more efficient LDMs as generative priors. The setup for LDMs is the following: given an image $\mathbf{x} \in \mathbb{R}^n$, we have an encoder $\mathcal{E} : \mathbb{R}^n \rightarrow \mathbb{R}^k$ and a decoder $\mathcal{D} : \mathbb{R}^k \rightarrow \mathbb{R}^n$ where $k \ll n$. Let $\mathbf{z} = \mathcal{E}(\mathbf{x}) \in \mathbb{R}^k$ denote the embedded samples in the latent space. One way of incorporating LDMs to solve inverse problems would be to replace the

update steps in Equation (6) with

$$\mathbf{z}'_{t-1} = \sqrt{\bar{\alpha}_{t-1}} \hat{\mathbf{z}}_0(\mathbf{z}_t) + \sqrt{1 - \bar{\alpha}_{t-1} - \eta \delta_t^2} \mathbf{s}_\theta(\mathbf{z}_t, t) + \eta \delta_t \boldsymbol{\epsilon}, \quad (8)$$

$$\mathbf{z}_{t-1} = \mathbf{z}'_{t-1} - \zeta \nabla_{\mathbf{z}_t} \|\mathbf{y} - \mathcal{A}(\mathcal{D}(\hat{\mathbf{z}}_0(\mathbf{z}_t)))\|_2^2, \quad (9)$$

After incorporating LDMs, this can be viewed as a non-linear inverse problem due to the non-linearity of the decoder $\mathcal{D}(\cdot)$. As this builds upon the idea behind DPS, we refer to this algorithm as *Latent-DPS*. While this formulation seems to work, we empirically observe that Latent-DPS often produces reconstructions that are often noisy or blurry and inconsistent with the measurements. We conjecture that since the forward operator involving the decoder is highly nonconvex, the gradient update may lead towards a local minimum.

3. ReSample: Inverse Problems using Latent Diffusion Models

3.1. Proposed Method

Hard Data Consistency. Similar to Latent-DPS, our algorithm involves incorporating data consistency into the reverse sampling process of LDMs. However, instead of a gradient-like update as shown in Equation (9), we propose to solve an optimization problem on *some time steps* t of the reverse process:

$$\hat{\mathbf{z}}_0(\mathbf{y}) \in \arg \min_{\mathbf{z}} \frac{1}{2} \|\mathbf{y} - \mathcal{A}(\mathcal{D}(\mathbf{z}))\|_2^2, \quad (10)$$

where we denote $\hat{\mathbf{z}}_0(\mathbf{y})$ as the sample consistent with the measurements $\mathbf{y} \in \mathbb{R}^m$. One can solve Equation (10) using iterative solvers such as gradient descent, but instead of starting at some random initial point, we initialize using $\hat{\mathbf{z}}_0(\mathbf{z}_t)$, where $\hat{\mathbf{z}}_0(\mathbf{z}_t)$ is an estimate of the ground-truth latent sample at time t . The intuition behind this initialization is that we want to start the optimization process within local proximity of the global solution of Equation (10), to prevent resulting in a local minimum. We term this overall concept as *hard data consistency*, as we strictly enforce the measurements via optimization, rather than a “soft” approach through gradient update like Latent-DPS. To obtain $\hat{\mathbf{z}}_0(\mathbf{z}_t)$, we use Tweedie’s formula that gives us an approximation of the posterior mean which takes the following formula:

$$\hat{\mathbf{z}}_0(\mathbf{z}_t) = \mathbb{E}[\mathbf{z}_0 | \mathbf{z}_t] = \frac{1}{\sqrt{\bar{\alpha}_t}} (\mathbf{z}_t + (1 - \bar{\alpha}_t) \nabla \log p(\mathbf{z}_t)). \quad (11)$$

However, we would like to note that performing hard data consistency on every reverse sampling iteration t may be very costly. To address this, we first observe that as we approach $t = T$, the estimated $\hat{\mathbf{z}}_0(\mathbf{z}_t)$ can deviate significantly from the ground truth. In this regime, we find that hard data consistency provides only marginal benefits. Additionally, in the literature, existing works point out the existence of a three-stage phenomenon [28], where they demonstrate that data consistency is primarily beneficial for the semantic and refinement stages (the latter two stages when t is closer to 0) of the sampling process. Following this reasoning, we divide T into three sub-intervals and only apply the optimization in the latter two intervals. This approach provides both computational efficiency and accurate estimates of $\hat{\mathbf{z}}_0(\mathbf{z}_t)$.

Furthermore, even during these two intervals, we observe that we do not need to solve the optimization problem on every iteration t . Because of the continuity of the sampling process, after each data-consistency optimization step, the samples in the following steps can still remain similar semantic or structural information to some extent. Thus, we “reinforce” the data consistency constraint during the sampling process via a skipped-step mechanism. Empirically, we see that it is

Algorithm 1 ReSample: Solving Inverse Problems with Latent Diffusion Models

Require: Measurements \mathbf{y} , $\mathcal{A}(\cdot)$, Encoder $\mathcal{E}(\cdot)$, Decoder $\mathcal{D}(\cdot)$, Score function $s_\theta(\cdot, t)$, Pretrained LDM Parameters $\beta_t, \bar{\alpha}_t, \eta, \delta$, Hyperparameter γ to control σ_t^2 , Time steps to perform resample C

```

 $\mathbf{z}_T \sim \mathcal{N}(\mathbf{0}, \mathbf{I})$  ▷ Initial noise vector
for  $t = T - 1, \dots, 0$  do
   $\epsilon_1 \sim \mathcal{N}(\mathbf{0}, \mathbf{I})$ 
   $\hat{\mathbf{z}}_0 = \frac{1}{\sqrt{\bar{\alpha}_{t+1}}}(\mathbf{z}_{t+1} + \sqrt{1 - \bar{\alpha}_{t+1}}s_\theta(\mathbf{z}_{t+1}, t + 1))$  ▷ Predict  $\hat{\mathbf{z}}_0$ 
   $\mathbf{z}'_t = \sqrt{\bar{\alpha}_t}\hat{\mathbf{z}}_0 + \sqrt{1 - \bar{\alpha}_t - \eta\delta^2}s_\theta(\mathbf{z}_{t+1}, t + 1) + \eta\delta\epsilon_1$  ▷ Unconditional DDIM step
  if  $t \in C$  then
     $\hat{\mathbf{z}}_0(\mathbf{z}_t) = \frac{1}{\sqrt{\bar{\alpha}_t}}(\mathbf{z}'_t + \sqrt{(1 - \bar{\alpha}_t)}s_\theta(\mathbf{z}'_t, t))$  ▷ Use Tweedie's formula
     $\hat{\mathbf{z}}_0(\mathbf{y}) \in \arg \min_{\mathbf{z}} \frac{1}{2}\|\mathbf{y} - \mathcal{A}(\mathcal{D}(\mathbf{z}))\|_2^2$  ▷ Solve with initial point  $\hat{\mathbf{z}}_0(\mathbf{z}_t)$ 
     $\mathbf{z}_t = \text{StochasticResample}(\hat{\mathbf{z}}_0(\mathbf{y}), \mathbf{z}'_t, \gamma)$  ▷ Map back to  $t$ 
  else
     $\mathbf{z}_t = \mathbf{z}'_t$  ▷ Unconditional sampling if not resampling
   $\mathbf{x}_0 = \mathcal{D}(\mathbf{z}_0)$  ▷ Output reconstructed image

```

sufficient to perform this on every 10 (or so) iterations of t . One can think of hard data consistency as guiding the sampling process towards the ground truth signal \mathbf{x}^* (or respectively \mathbf{z}^*) such that it is consistent with the given measurements. Lastly, in the presence of measurement noise, minimizing Equation (10) to zero loss can lead to overfitting the noise. To remedy this, we perform early stopping, where we only minimize up to a threshold τ based on the noise level. We will discuss the details of the optimization process in the Appendix. We also observe that an additional Latent-DPS step after unconditional sampling can (sometimes) marginally increase the overall performance. We perform an ablation study on the performance of including Latent-DPS in the Appendix.

Remapping Back to \mathbf{z}_t . Following the flowchart in Figure 2, the next step is to map the measurement-consistent sample $\hat{\mathbf{z}}_0(\mathbf{y})$ back onto the data manifold defined by the noisy samples at time t to continue the reverse sampling process. Doing so would be equivalent to computing the posterior distribution $p(\mathbf{z}_t|\mathbf{y})$. To incorporate $\hat{\mathbf{z}}_0(\mathbf{y})$ into the posterior, we propose to construct an auxiliary distribution $p(\hat{\mathbf{z}}_t|\hat{\mathbf{z}}_0(\mathbf{y}), \mathbf{y})$ in replace of $p(\mathbf{z}_t|\mathbf{y})$. Here, $\hat{\mathbf{z}}_t$ denotes the remapped sample and \mathbf{z}'_t denotes the unconditional sample before remapping. One simple way of computing this distribution to obtain $\hat{\mathbf{z}}_t$ is shown in Proposition 1.

Proposition 1 (Stochastic Encoding). *Since the sample $\hat{\mathbf{z}}_t$ given $\hat{\mathbf{z}}_0(\mathbf{y})$ and measurement \mathbf{y} is conditionally independent of \mathbf{y} , we have that*

$$p(\hat{\mathbf{z}}_t|\hat{\mathbf{z}}_0(\mathbf{y}), \mathbf{y}) = p(\hat{\mathbf{z}}_t|\hat{\mathbf{z}}_0(\mathbf{y})) = \mathcal{N}(\sqrt{\bar{\alpha}_t}\hat{\mathbf{z}}_0(\mathbf{y}), (1 - \bar{\alpha}_t)\mathbf{I}). \quad (12)$$

We defer all of the proofs to the Appendix. Proposition 1 provides us a way of computing $\hat{\mathbf{z}}_t$, which we refer to as *stochastic encoding*. However, we observe that using stochastic encoding can incur a high variance when t is farther away from $t = 0$, where the ground truth signal exists. This large variance can often lead to noisy image reconstructions. To address this issue, we propose a posterior sampling technique that reduces the variance by additionally conditioning on \mathbf{z}'_t , the unconditional sample at time t . Here, the intuition is that by using information of \mathbf{z}'_t , we can get closer to the ground truth \mathbf{z}_t , which effectively reduces the variance. In Lemma 2, under some mild assumptions, we show that this new distribution $p(\hat{\mathbf{z}}_t|\mathbf{z}'_t, \hat{\mathbf{z}}_0(\mathbf{y}), \mathbf{y})$ is a tractable Gaussian distribution.

Proposition 2 (Stochastic Resampling). *Suppose that $p(\mathbf{z}'_t|\hat{\mathbf{z}}_t, \hat{\mathbf{z}}_0(\mathbf{y}), \mathbf{y})$ is normally distributed such that $p(\mathbf{z}'_t|\hat{\mathbf{z}}_t, \hat{\mathbf{z}}_0(\mathbf{y}), \mathbf{y}) = \mathcal{N}(\boldsymbol{\mu}_t, \sigma_t^2)$. If we let $p(\hat{\mathbf{z}}_t|\hat{\mathbf{z}}_0(\mathbf{y}), \mathbf{y})$ be a prior for $\boldsymbol{\mu}_t$, then the posterior distribution*

Method	Super Resolution 4×			Inpainting (Random 70%)		
	LPIPS↓	PSNR↑	SSIM↑	LPIPS↓	PSNR↑	SSIM↑
DPS [11]	0.173 ± 0.04	28.41 ± 2.20	0.782 ± 0.06	<u>0.102</u> ± 0.02	<u>32.48</u> ± 2.30	<u>0.899</u> ± 0.03
MCG [12]	0.193 ± 0.03	25.92 ± 2.35	0.740 ± 0.05	0.134 ± 0.03	29.53 ± 2.70	0.847 ± 0.05
ADMM-PnP [29]	0.304 ± 0.04	21.08 ± 3.13	0.631 ± 0.11	0.627 ± 0.07	15.40 ± 2.09	0.342 ± 0.09
DDRM [13]	0.151 ± 0.03	<u>29.49</u> ± 1.93	0.817 ± 0.05	0.166 ± 0.03	27.69 ± 1.54	0.798 ± 0.04
DMPS [16]	<u>0.147</u> ± 0.03	28.48 ± 1.92	<u>0.811</u> ± 0.05	0.175 ± 0.03	28.84 ± 1.65	0.826 ± 0.03
Latent-DPS	0.272 ± 0.05	26.83 ± 2.00	0.690 ± 0.07	0.226 ± 0.04	26.23 ± 1.84	0.703 ± 0.07
PSLD [21]	0.616 ± 0.13	15.54 ± 3.82	0.183 ± 0.07	0.260 ± 0.08	27.07 ± 2.45	0.689 ± 0.11
ReSample (Ours)	0.144 ± 0.029	30.45 ± 2.09	0.832 ± 0.05	0.082 ± 0.02	32.77 ± 2.23	0.903 ± 0.03

Table 1: **Quantitative results of super resolution and inpainting on the CelebA-HQ dataset.** Input images have an additive Gaussian noise with $\sigma_y = 0.01$. Best results are in bold and second best results are underlined.

$p(\hat{z}_t|z'_t, \hat{z}_0(\mathbf{y}), \mathbf{y})$ is given by

$$p(\hat{z}_t|z'_t, \hat{z}_0(\mathbf{y}), \mathbf{y}) = \mathcal{N}\left(\frac{\sigma_t^2 \sqrt{\bar{\alpha}_t} \hat{z}_0(\mathbf{y}) + (1 - \bar{\alpha}_t) z'_t}{\sigma_t^2 + (1 - \bar{\alpha}_t)}, \frac{\sigma_t^2 (1 - \bar{\alpha}_t)}{\sigma_t^2 + (1 - \bar{\alpha}_t)} \mathbf{I}\right). \quad (13)$$

We refer to this new mapping technique as *stochastic resampling*. Since we do not have access to σ_t^2 , it serves as a hyperparameter that we tune in our algorithm. The choice of σ_t^2 plays a role of controlling the tradeoff between prior consistency and data consistency. If $\sigma_t^2 \rightarrow 0$, then we recover unconditional sampling, and if $\sigma_t^2 \rightarrow \infty$, we recover stochastic encoding. We observe that this new technique also has several desirable properties, for which we rigorously prove in the next section.

3.2. Theoretical Results

In Section 3.1, we discussed that stochastic resampling induces less variance than stochastic encoding. Here, we aim to rigorously prove the validity of this statement.

Lemma 1. Let \tilde{z}_t and \hat{z}_t denote the stochastically encoded and resampled image of $\hat{z}_0(\mathbf{y})$, respectively. If $\text{VAR}(z'_t) > 0$, then we have that $\text{VAR}(\hat{z}_t) < \text{VAR}(\tilde{z}_t)$.

Theorem 1. If $\hat{z}_0(\mathbf{y})$ is measurement-consistent such that $\mathbf{y} = \mathcal{A}(\mathcal{D}(\hat{z}_0(\mathbf{y})))$, i.e. $\hat{z}_0 = \hat{z}_0(z_t) = \hat{z}_0(\mathbf{y})$, then stochastic resample is unbiased such that $\mathbb{E}[\hat{z}_t|\mathbf{y}] = \mathbb{E}[z'_t]$.

These two results, Lemma 1 and Theorem 1, prove the benefits of stochastic resampling. At a high-level, these proofs rely on the fact the posterior distributions of both stochastic encoding and resampling are Gaussian and compare their respective means and variances. In the following result, we characterize the variance induced by stochastic resampling, and show that as $t \rightarrow 0$, the variance decreases, giving us a reconstructed image that is of better quality.

Theorem 2. Let z_0 denote a sample from the data distribution and z_t be a sample from the noisy perturbed distribution at time t . Then,

$$\text{Cov}(z_0|z_t) = \frac{(1 - \bar{\alpha}_t)^2}{\bar{\alpha}_t} \nabla_{z_t}^2 \log p_{z_t}(z_t) + \frac{1 - \bar{\alpha}_t}{\bar{\alpha}_t} \mathbf{I}.$$

By Theorem 2, notice that since as α_t is an increasing sequence that converges to 1 as t decreases, the variance between the ground truth z_0 and the estimated \hat{z}_0 decreases to 0 as $t \rightarrow 0$, assuming that $\nabla_{z_t}^2 \log p_{z_t}(z_t) < \infty$. Following our theory, we empirically show that stochastic resampling can reconstruct signals that are less noisy than stochastic encoding, as shown in the next section.

4. Experiments

We conduct experiments to solve both linear and nonlinear inverse problems on natural and medical images. We compare our algorithm to several state-of-the-art methods that directly use the pixel

Method	Nonlinear Deblurring			Gaussian Deblurring		
	LPIPS↓	PSNR↑	SSIM↑	LPIPS↓	PSNR↑	SSIM↑
DPS [11]	0.230 ± 0.065	<u>26.81</u> ± 2.84	<u>0.720</u> ± 0.077	0.175 ± 0.03	28.36 ± 2.12	0.772 ± 0.07
MCG [12]	-	-	-	0.517 ± 0.06	15.85 ± 1.08	0.536 ± 0.08
ADMM-PnP [29]	0.499 ± 0.073	16.17 ± 4.01	0.359 ± 0.140	0.289 ± 0.04	20.98 ± 4.51	0.602 ± 0.15
DDRM [13]	-	-	-	0.193 ± 0.04	26.88 ± 1.96	0.747 ± 0.07
DMPS [16]	-	-	-	0.206 ± 0.04	26.45 ± 1.83	0.726 ± 0.07
Latent-DPS	<u>0.225</u> ± 0.04	26.18 ± 1.73	0.703 ± 0.07	0.205 ± 0.04	27.42 ± 1.84	0.729 ± 0.07
PSLD [21]	-	-	-	0.360 ± 0.15	23.07 ± 3.91	0.494 ± 0.22
ReSample (Ours)	0.153 ± 0.03	30.18 ± 2.21	0.828 ± 0.05	0.148 ± 0.04	30.69 ± 2.14	0.832 ± 0.05

Table 2: **Quantitative results of Gaussian and nonlinear deblurring on the CelebA-HQ dataset.** Input images have an additive Gaussian noise with $\sigma_y = 0.01$. Best results are in bold and second best results are underlined. For nonlinear deblurring, some baselines are omitted, as they can only solve *linear* inverse problems.

space: DPS [11], Manifold Constrained Gradients (MCG) [12], Denoising Diffusion Destoration Models (DDRM) [13], Diffusion Model Posterior Sampling (DMPS) [16], and plug-and-play using ADMM (ADMM-PnP) [29]. We also compare our algorithm to Latent-DPS and Posterior Sampling with Latent Diffusion (PSLD) [21], a concurrent work we recently notice also tackling latent diffusion models. Various quantitative metrics are used for evaluation including Learned Perceptual Image Patch Similarity (LPIPS) distance, peak signal-to-noise-ratio (PSNR), and structural similarity index (SSIM). Lastly, we conduct ablation study to compare the performance of stochastic encoding and our proposed stochastic resampling technique as mentioned in Section 3.1, and also demonstrate the memory efficiency gained by leveraging LDMs.

4.1. Experimental Results

Experiments on Natural Images. For the experiments on natural images, we use datasets FFHQ [30], CelebA-HQ [31], and LSUN-Bedroom [32] with the image resolution of $256 \times 256 \times 3$. We take pre-trained latent diffusion models LDM-VQ4 trained on FFHQ and CelebA-HQ provided by Rombach et al. [19] with autoencoders that yield images of size $64 \times 64 \times 3$, and DDPMs [22] also trained on FFHQ and CelebA-HQ training sets. Then, we sample 100 images from both the FFHQ and CelebA-HQ validation sets for testing evaluation. For computing quantitative results, all images are normalized to the range $[0, 1]$. All experiments had Gaussian measurement noise with standard deviation $\sigma_y = 0.01$. Due to limited space, we put the results on FFHQ and details of the hyperparameters to the Appendix.

For linear inverse problems, we consider the following tasks: (1) Gaussian deblurring, (2) inpainting (with a random mask), and (3) super resolution. For Gaussian deblurring, we use a kernel with size 61×61 with standard deviation 3.0. For super resolution, we use bicubic downsampling and a random mask with varying levels of missing pixels for inpainting. For nonlinear inverse problems, we consider nonlinear deblurring as proposed by Chung et al. [11]. The quantitative results are displayed in Tables 1 and 2, with qualitative results in Figure 3. In Tables 1 and 2, we can see that ReSample significantly outperforms all of the baselines across all three metrics on the CelebA-HQ dataset. We also observe that ReSample performs better than or comparable to all baselines on the FFHQ dataset as shown in the Appendix. Interestingly, we observe that PSLD [21] seems to struggle in the presence of measurement noise, often resulting in reconstructions that underperform compared to pixel-based methods. Remarkably, our method excels in handling nonlinear inverse problems, further demonstrating the flexibility of our algorithm. We further demonstrate

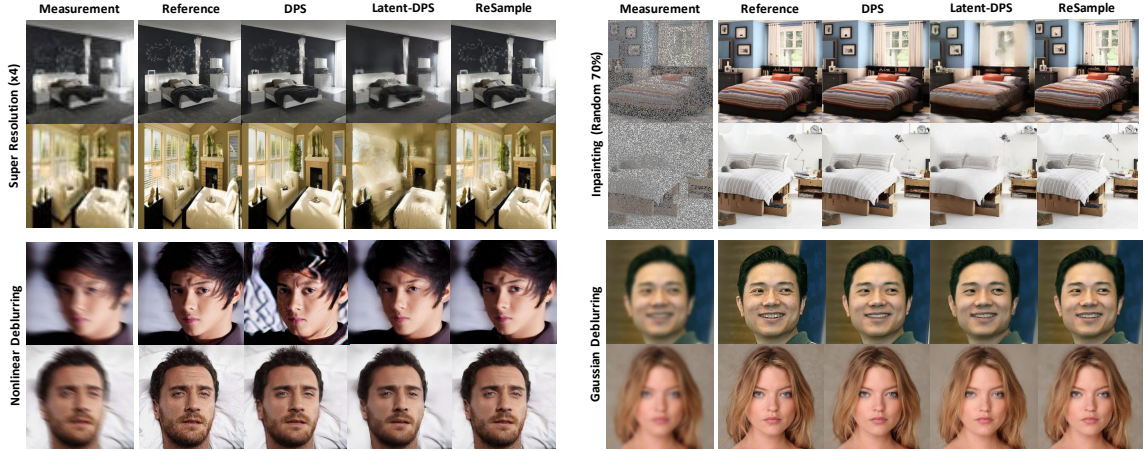


Figure 3: **Qualitative results of multiple tasks on the LSUN-Bedroom and CelebA-HQ datasets.** All inverse problems have Gaussian measurement noise with variance $\sigma_y = 0.01$.

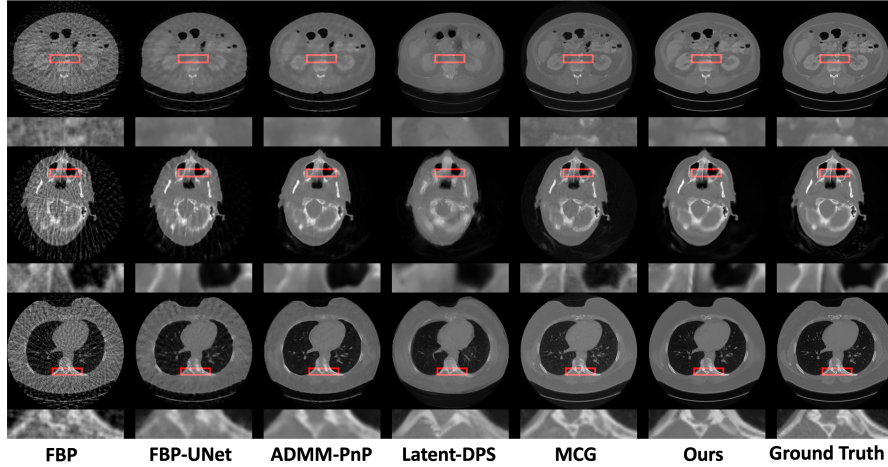


Figure 4: **Qualitative results of CT reconstruction on the LDCT dataset.** We annotate the critical image structures in a red box, and zoom in below the image.

Method	Abdominal		Head		Chest	
	PSNR \uparrow	SSIM \uparrow	PSNR \uparrow	SSIM \uparrow	PSNR \uparrow	SSIM \uparrow
Latent-DPS	26.80 \pm 1.09	0.870 \pm 0.026	28.64 \pm 5.38	0.893 \pm 0.058	25.67 \pm 1.14	0.822 \pm 0.033
MCG [12]	29.41 \pm 3.14	0.857 \pm 0.041	28.28 \pm 3.08	0.795 \pm 0.116	27.92 \pm 2.48	0.842 \pm 0.036
DPS [11]	27.33 \pm 2.68	0.715 \pm 0.031	24.51 \pm 2.77	0.665 \pm 0.058	24.73 \pm 1.84	0.682 \pm 0.113
PnP-UNet [33]	32.84 \pm 1.29	0.942 \pm 0.008	33.45 \pm 3.25	0.945 \pm 0.023	29.67 \pm 1.14	0.891 \pm 0.011
FBP	26.29 \pm 1.24	0.727 \pm 0.036	26.71 \pm 5.02	0.725 \pm 0.106	24.12 \pm 1.14	0.655 \pm 0.033
FBP-UNet [34]	32.77 \pm 1.21	0.937 \pm 0.013	31.95 \pm 3.32	0.917 \pm 0.048	<u>29.78</u> \pm 1.12	0.885 \pm 0.016
ReSample (Ours)	35.91 \pm 1.22	0.965 \pm 0.007	37.82 \pm 5.31	0.978 \pm 0.014	31.72 \pm 0.912	0.922 \pm 0.011

Table 3: **Quantitative results of CT reconstruction on the LDCT dataset.** Best results are in bold and second best results are underlined.

the superiority of ReSample for handling nonlinear inverse problems in Figure 6, where we show that we can consistently outperform DPS.

Experiments on Medical Images. For experiments on medical images, we fine-tune LDMs on 2000 2D computed tomography (CT) images with image resolution of 256×256 , randomly sampled from the AAPM LDCT dataset [35] of 40 patients, and test on the 300 2D CT images from the remaining 10 patients. We take the FFHQ LDM-VQ4 model provided by Rombach et al. [19] as pre-trained latent diffusion model in this experimental setting followed by 100K fine-tuning iterations. Then, we

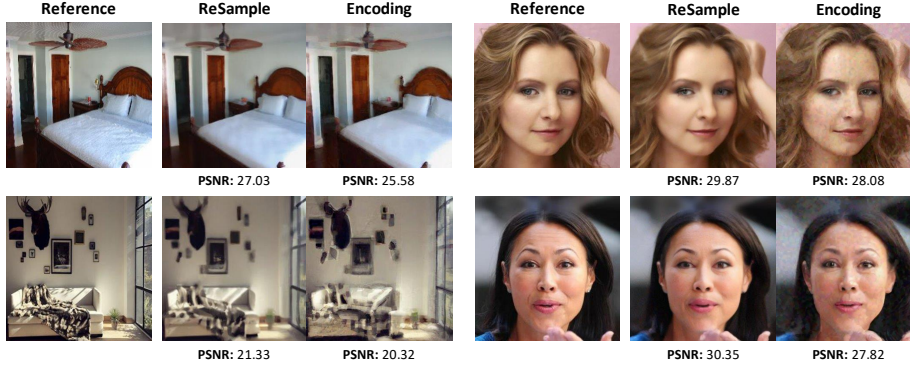


Figure 5: **Effectiveness of our resampling technique compared to stochastic encoding.** Results were demonstrated on the LSUN-Bedroom and CelebA-HQ datasets with measurement noise of $\sigma_y = 0.05$ to highlight the effectiveness of stochastic resample.

simulate CT measurements (sinograms) with a parallel-beam geometry using 25 projection angles equally distributed across 180 degrees using the torch-radon package [36]. Following the natural images, the sinograms were perturbed with additive Gaussian measurement noise with $\sigma_y = 0.01$. Along with the baselines used in the natural image experiments, we also compare to the following methods: (1) Filtered Backprojection (FBP), which is a standard conventional CT reconstruction technique, and (2) FBP-UNet, a supervised learning method that maps the FBP reconstructed images to ground truth images using a UNet model. For FBP-UNet and PnP-UNet, we trained a model on 3480 2D CT from the training set. For MCG and DPS, we used the pre-trained checkpoints provided by Chung et al. [12]. We present visual reconstructions with highlighted critical anatomic structures in Figure 4 and quantitative results in Table 3. Here, we observe that our algorithm outperforms all of the baselines in terms of PSNR and SSIM. Visually, we also observe that our algorithm is able to reconstruct smoother images that have more accurate and sharper details.

4.2. Ablation Studies

Effectiveness of the Resampling Technique. Here, we validate our theoretical results by conducting ablation studies on stochastic resampling. Specifically, we perform experiments on the LSUN-Bedroom and CelebA-HQ datasets with tasks of Gaussian deblurring and super-resolution. As shown in Figure 5, we observe that stochastic resampling reconstructs smoother images with higher PSNRs compared to stochastic encoding, corroborating our theory.

Effectiveness of Hard Data Consistency. In Figure 6, we perform an ablation study on the ReSample frequency on CT reconstruction. This observation is in line with what we expect intuitively, as more ReSample time steps (i.e., more data consistency) lead to more accurate reconstructions. More specifically, we observe in Figure 6 (right) that if we perform more iterations of ReSample, we obtain reconstructions with higher PSNR.

Memory Efficiency. To demonstrate the memory efficiency of our algorithm, we use the command `nvidia-smi` to monitor the memory consumption during solving an inverse problem, in comparison to our baselines. We present

Table 4: Memory Usage of Different Methods for Gaussian Deblurring on the FFHQ Dataset

Model	Algorithm	Model Only	Memory Increment	Total
DDPM	DPS	1953MB	+3416MB (175%)	5369MB
	MCG		+3421MB (175%)	5374MB
	DMPs		+5215MB (267 %)	7168MB
	DDRM		+18833MB (964 %)	20786MB
LDM	PSLD	3969MB	+5516MB (140%)	9485MB
	ReSample		+1040MB (26.2%)	5009MB

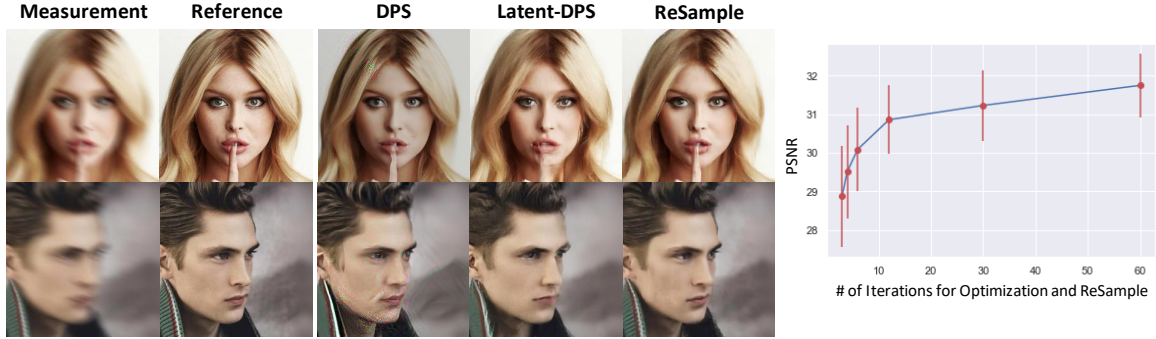


Figure 6: **Additional results on the performance of ReSample.** Left: Results on nonlinear deblurring highlighting the performance of ReSample. Right: Ablation study on the ReSample frequency on the performance.

the memory usage for Gaussian deblurring on the FFHQ dataset in Table 4. Although the entire LDM models occupy more memory due to the autoencoders, our algorithm itself exhibits memory efficiency, resulting in lower overall memory usage. This underscores its potential in domains like medical imaging, where memory complexity plays a crucial role in feasibility.

5. Conclusion

In this paper, we propose *ReSample*, an algorithm that can effectively leverage LDMs to solve *general* inverse problems. We demonstrated that (1) our algorithm can reconstruct high-quality images compared to many baselines and (2) we can fine-tune existing models for medical imaging tasks and achieve an additional reduction in memory usage. One fundamental limitation of our method lies in the computational overhead of hard data consistency, which we leave as a significant challenge for future work to address and improve upon.

6. Acknowledgement

BS and LS acknowledge support from U-M MIDAS PODS Grant and MICDE Catalyst Grant, and computing resource support from Google Cloud Research Credits Program. SMK and QQ acknowledge support from U-M START & PODS grants, NSF CAREER CCF-2143904, NSF CCF-2212066, NSF CCF-2212326, ONR N00014-22-1-2529, AWS AI Award, and a gift grant from KLA.

References

- [1] Amir Beck and Marc Teboulle. A fast iterative shrinkage-thresholding algorithm for linear inverse problems. *SIAM Journal on Imaging Sciences*, 2(1):183–202, 2009. doi: 10.1137/080716542. URL <https://doi.org/10.1137/080716542>.
- [2] Manyá V. Afonso, José M. Bioucas-Dias, and Mário A. T. Figueiredo. An augmented lagrangian approach to the constrained optimization formulation of imaging inverse problems. *IEEE Transactions on Image Processing*, 20(3):681–695, 2011. doi: 10.1109/TIP.2010.2076294.
- [3] Paul Suetens. *Fundamentals of medical imaging*. Cambridge university press, 2017.
- [4] Saiprasad Ravishankar, Jong Chul Ye, and Jeffrey A Fessler. Image reconstruction: From sparsity to data-adaptive methods and machine learning. *Proceedings of the IEEE*, 108(1):86–109, 2019.
- [5] Wei Liu, Xin Xia, Lu Xiong, Yishi Lu, Letian Gao, and Zhuoping Yu. Automated vehicle sideslip angle estimation considering signal measurement characteristic. *IEEE Sensors Journal*, 21(19): 21675–21687, 2021.
- [6] Wei Liu, Karoll Quijano, and Melba M Crawford. Yolov5-tassel: detecting tassels in rgb uav imagery with improved yolov5 based on transfer learning. *IEEE Journal of Selected Topics in Applied Earth Observations and Remote Sensing*, 15:8085–8094, 2022.
- [7] Prafulla Dhariwal and Alexander Nichol. Diffusion models beat gans on image synthesis. *Advances in Neural Information Processing Systems*, 34:8780–8794, 2021.
- [8] Tero Karras, Miika Aittala, Timo Aila, and Samuli Laine. Elucidating the design space of diffusion-based generative models. *arXiv preprint arXiv:2206.00364*, 2022.
- [9] Yang Song, Prafulla Dhariwal, Mark Chen, and Ilya Sutskever. Consistency models. *arXiv preprint arXiv:2303.01469*, 2023.
- [10] Yang Song, Liye Shen, Lei Xing, and Stefano Ermon. Solving inverse problems in medical imaging with score-based generative models. *International Conference on Learning Representations*, 2022. URL <https://openreview.net/forum?id=vaRCHVj0uGI>.
- [11] Hyungjin Chung, Jeongsol Kim, Michael Thompson Mccann, Marc Louis Klasky, and Jong Chul Ye. Diffusion posterior sampling for general noisy inverse problems. In *The Eleventh International Conference on Learning Representations*, 2023. URL <https://openreview.net/forum?id=OnD9zGAGT0k>.
- [12] Hyungjin Chung, Byeongsu Sim, Dohoon Ryu, and Jong Chul Ye. Improving diffusion models for inverse problems using manifold constraints. *arXiv preprint arXiv:2206.00941*, 2022.
- [13] Bahjat Kwar, Michael Elad, Stefano Ermon, and Jiaming Song. Denoising diffusion restoration models. *arXiv preprint arXiv:2201.11793*, 2022.
- [14] Jiaming Song, Arash Vahdat, Morteza Mardani, and Jan Kautz. Pseudoinverse-guided diffusion models for inverse problems. In *International Conference on Learning Representations*, 2023.
- [15] Hyungjin Chung, Suhyeon Lee, and Jong Chul Ye. Fast diffusion sampler for inverse problems by geometric decomposition. *arXiv preprint arXiv:2303.05754*, 2023.

- [16] Xiangming Meng and Yoshiyuki Kabashima. Diffusion model based posterior sampling for noisy linear inverse problems. *arXiv preprint arXiv:2211.12343*, 2022.
- [17] Dan Zhang and Fangfang Zhou. Self-supervised image denoising for real-world images with context-aware transformer. *IEEE Access*, 11:14340–14349, 2023.
- [18] Michael Lustig, David Donoho, and John M Pauly. Sparse mri: The application of compressed sensing for rapid mr imaging. *Magnetic Resonance in Medicine: An Official Journal of the International Society for Magnetic Resonance in Medicine*, 58(6):1182–1195, 2007.
- [19] Robin Rombach, Andreas Blattmann, Dominik Lorenz, Patrick Esser, and Björn Ommer. High-resolution image synthesis with latent diffusion models. In *Proceedings of the IEEE/CVF Conference on Computer Vision and Pattern Recognition*, pages 10684–10695, 2022.
- [20] Arash Vahdat, Karsten Kreis, and Jan Kautz. Score-based generative modeling in latent space. In M. Ranzato, A. Beygelzimer, Y. Dauphin, P.S. Liang, and J. Wortman Vaughan, editors, *Advances in Neural Information Processing Systems*, volume 34, pages 11287–11302. Curran Associates, Inc., 2021. URL https://proceedings.neurips.cc/paper_files/paper/2021/file/5dca4c6b9e244d24a30b4c45601d9720-Paper.pdf.
- [21] Litu Rout, Negin Raoof, Giannis Daras, Constantine Caramanis, Alexandros G. Dimakis, and Sanjay Shakkottai. Solving linear inverse problems provably via posterior sampling with latent diffusion models. *arXiv preprint arXiv:2307.00619*, 2023.
- [22] Jonathan Ho, Ajay Jain, and Pieter Abbeel. Denoising diffusion probabilistic models. *Advances in Neural Information Processing Systems*, 33:6840–6851, 2020.
- [23] Yang Song, Jascha Sohl-Dickstein, Diederik P. Kingma, Abhishek Kumar, Stefano Ermon, and Ben Poole. Score-based generative modeling through stochastic differential equations. *arXiv preprint arXiv:2011.13456*, 2021.
- [24] Pascal Vincent. A connection between score matching and denoising autoencoders. *Neural Computation*, 23(7):1661–1674, 2011. doi: 10.1162/NECO_a_00142.
- [25] Jiaming Song, Chenlin Meng, and Stefano Ermon. Denoising diffusion implicit models. *arXiv preprint arXiv:2010.02502*, 2020.
- [26] Cheng Lu, Yuhao Zhou, Fan Bao, Jianfei Chen, Chongxuan Li, and Jun Zhu. Dpm-solver: A fast ode solver for diffusion probabilistic model sampling in around 10 steps. *arXiv preprint arXiv:2206.00927*, 2022.
- [27] Yinhuai Wang, Jiwen Yu, and Jian Zhang. Zero-shot image restoration using denoising diffusion null-space model. *arXiv preprint arXiv:2212.00490*, 2022.
- [28] Jiwen Yu, Yinhuai Wang, Chen Zhao, Bernard Ghanem, and Jian Zhang. Freedom: Training-free energy-guided conditional diffusion model. *arXiv preprint arXiv:2303.09833*, 2023.
- [29] Rizwan Ahmad, Charles A Bouman, Gregory T Buzzard, Stanley H Chan, Edward T Reehorst, and Philip Schniter. Plug and play methods for magnetic resonance imaging. 2019.
- [30] Vahid Kazemi and Josephine Sullivan. One millisecond face alignment with an ensemble of regression trees. In *2014 IEEE Conference on Computer Vision and Pattern Recognition*, pages 1867–1874, 2014. doi: 10.1109/CVPR.2014.241.

- [31] Ziwei Liu, Ping Luo, Xiaogang Wang, and Xiaoou Tang. Deep learning face attributes in the wild. In *Proceedings of International Conference on Computer Vision (ICCV)*, 2015.
- [32] Fisher Yu, Ari Seff, Yinda Zhang, Shuran Song, Thomas Funkhouser, and Jianxiong Xiao. Lsun: Construction of a large-scale image dataset using deep learning with humans in the loop. *arXiv preprint arXiv:1506.03365*, 2016.
- [33] Davis Gilton, Gregory Ongie, and Rebecca Willett. Model adaptation for inverse problems in imaging. *IEEE Transactions on Computational Imaging*, 7:661–674, 2021.
- [34] Kyong Hwan Jin, Michael T McCann, Emmanuel Froustey, and Michael Unser. Deep convolutional neural network for inverse problems in imaging. *IEEE Transactions on Image Processing*, 26(9):4509–4522, 2017.
- [35] Taylor R Moen, Baiyu Chen, David R Holmes III, Xinhui Duan, Zhicong Yu, Lifeng Yu, Shuai Leng, Joel G Fletcher, and Cynthia H McCollough. Low-dose ct image and projection dataset. *Medical physics*, 48(2):902–911, 2021.
- [36] Matteo Ronchetti. Torchradon: Fast differentiable routines for computed tomography. *arXiv preprint arXiv:2009.14788*, 2020.
- [37] Viraj Shah, Rakib Hyder, M. Salman Asif, and Chinmay Hegde. Provably convergent algorithms for solving inverse problems using generative models. *arXiv preprint arXiv:2105.06371*, 2021.
- [38] Kai Zhang, Wangmeng Zuo, Yunjin Chen, Deyu Meng, and Lei Zhang. Beyond a gaussian denoiser: Residual learning of deep cnn for image denoising. *IEEE transactions on image processing*, 26(7):3142–3155, 2017.
- [39] Paul A. Bromiley. Products and convolutions of gaussian probability density functions. 2013.

Appendix

In this section, we present additional experimental results to supplement those presented in the main paper. In Section A, we present additional qualitative and quantitative results to highlight the performance of ReSample. In Section B, we briefly discuss some of the implementation details regarding hard data consistency. In Section C, we outline all of the hyperparameters used to produce our results. In Section D, we discuss some more reasons to why Latent-DPS fails to consistently accurately recover the underlying image. Lastly, in Section E, we present our deferred proofs.

A. Additional Results

A.1. Results on FFHQ

Here, we provide additional quantitative results on the FFHQ dataset. Similar to the results in the main text on the CelebA-HQ dataset, ReSample outperforms the baselines across many different tasks.

Method	Super Resolution 4×			Inpainting (Random 70%)		
	LPIPS↓	PSNR↑	SSIM↑	LPIPS↓	PSNR↑	SSIM↑
DPS	0.175 ± 0.04	28.47 ± 2.09	0.793 ± 0.05	0.106 ± 0.03	32.32 ± 2.21	0.897 ± 0.04
MCG	0.223 ± 0.04	23.74 ± 3.18	0.673 ± 0.07	0.178 ± 0.03	24.89 ± 2.57	0.731 ± 0.06
ADMM-PnP	0.303 ± 0.03	21.30 ± 3.98	0.760 ± 0.04	0.308 ± 0.07	15.87 ± 2.09	0.608 ± 0.09
DDRM	0.257 ± 0.03	27.51 ± 1.79	0.753 ± 0.05	0.287 ± 0.03	24.97 ± 1.51	0.680 ± 0.05
DMPS	0.181 ± 0.03	27.21 ± 1.92	0.766 ± 0.06	0.150 ± 0.03	28.17 ± 1.58	0.814 ± 0.04
Latent-DPS	0.344 ± 0.05	24.65 ± 1.77	0.609 ± 0.07	0.270 ± 0.05	27.08 ± 1.97	0.727 ± 0.06
PSLD	0.580 ± 0.05	15.81 ± 1.54	0.183 ± 0.07	0.270 ± 0.06	25.61 ± 2.02	0.630 ± 0.09
ReSample (Ours)	0.164 ± 0.03	28.90 ± 1.86	0.804 ± 0.05	0.099 ± 0.02	<u>31.34</u> ± 2.11	<u>0.890</u> ± 0.03

Table 5: Comparison of quantitative results on inverse problems on the FFHQ dataset. Input images have an additive Gaussian noise with $\sigma_y = 0.01$. Best results are in bold and second best results are underlined.

Method	Nonlinear Deblurring			Gaussian Deblurring		
	LPIPS↓	PSNR↑	SSIM↑	LPIPS↓	PSNR↑	SSIM↑
DPS	0.197 ± 0.06	<u>27.13</u> ± 3.11	<u>0.762</u> ± 0.08	0.169 ± 0.04	27.70 ± 2.04	0.774 ± 0.05
MCG	-	-	-	0.371 ± 0.04	25.33 ± 1.74	0.668 ± 0.06
ADMM-PnP	0.424 ± 0.03	21.80 ± 1.42	0.497 ± 0.05	0.399 ± 0.03	21.23 ± 3.01	0.675 ± 0.06
DDRM	-	-	-	0.299 ± 0.039	26.51 ± 1.67	0.702 ± 0.06
DMPS	-	-	-	0.227 ± 0.036	26.04 ± 1.75	0.699 ± 0.066
Latent-DPS	0.319 ± 0.05	24.52 ± 1.75	0.637 ± 0.07	0.258 ± 0.05	25.98 ± 1.66	0.704 ± 0.06
PSLD	-	-	-	0.422 ± 0.11	20.08 ± 2.97	0.400 ± 0.16
ReSample (Ours)	0.171 ± 0.04	30.03 ± 1.78	0.838 ± 0.04	<u>0.201</u> ± 0.04	28.73 ± 1.87	0.794 ± 0.05

Table 6: Comparison of quantitative results on inverse problems on the FFHQ dataset. Input images have an additive Gaussian noise with $\sigma_y = 0.01$. Best results are in bold and second best results are underlined.

We observe that ReSample outperforms all baselines in nonlinear deblurring and super resolution, while demonstrating comparable performance to DPS [11] in Gaussian deblurring and inpainting. An interesting observation is that ReSample exhibits the largest performance gap from DPS in non-linear deblurring and the smallest performance gap in random inpainting, mirroring the pattern we observed in the results of the CelebA-HQ dataset. This may suggest that ReSample performs better than baselines when the forward operator is more complex.

A.2. Additional Qualitative Results

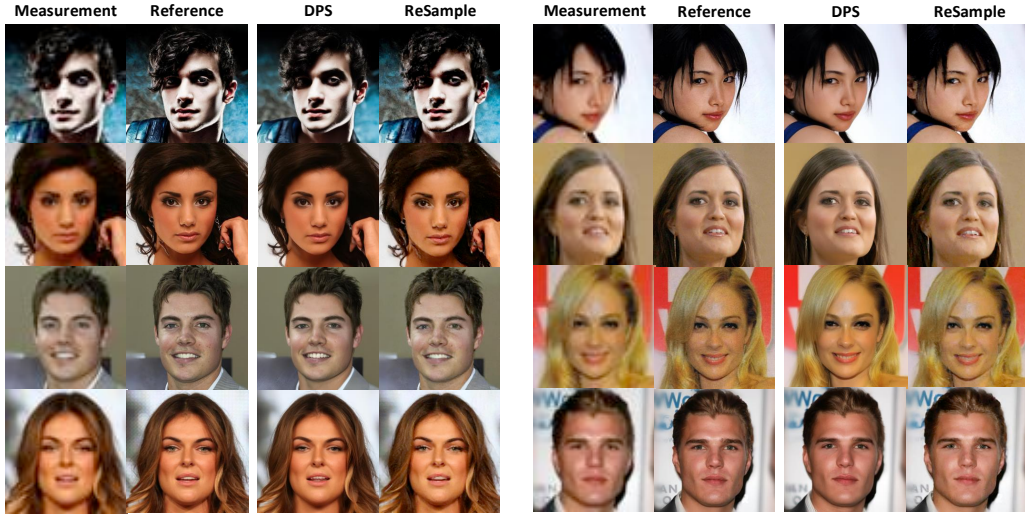


Figure 7: Additional results on super resolution ($4\times$) on the CelebA-HQ dataset with Gaussian measurement noise of variance $\sigma_y = 0.01$.

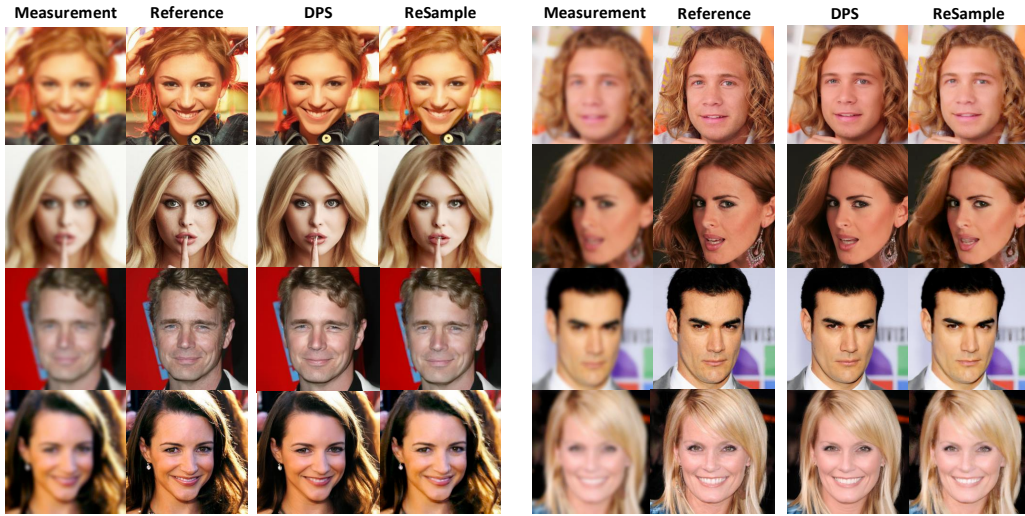


Figure 8: Additional results on Gaussian deblurring on the CelebA-HQ dataset with Gaussian measurement noise of variance $\sigma_y = 0.01$.

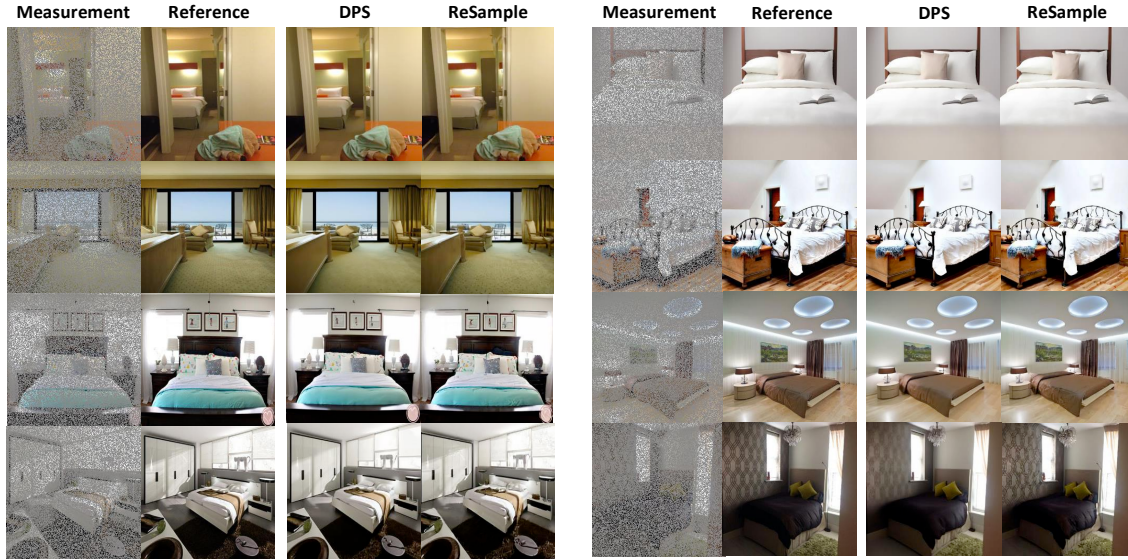


Figure 9: Additional results on inpainting with a random mask (70%) on the LSUN-Bedroom dataset with Gaussian measurement noise of variance $\sigma_y = 0.01$.

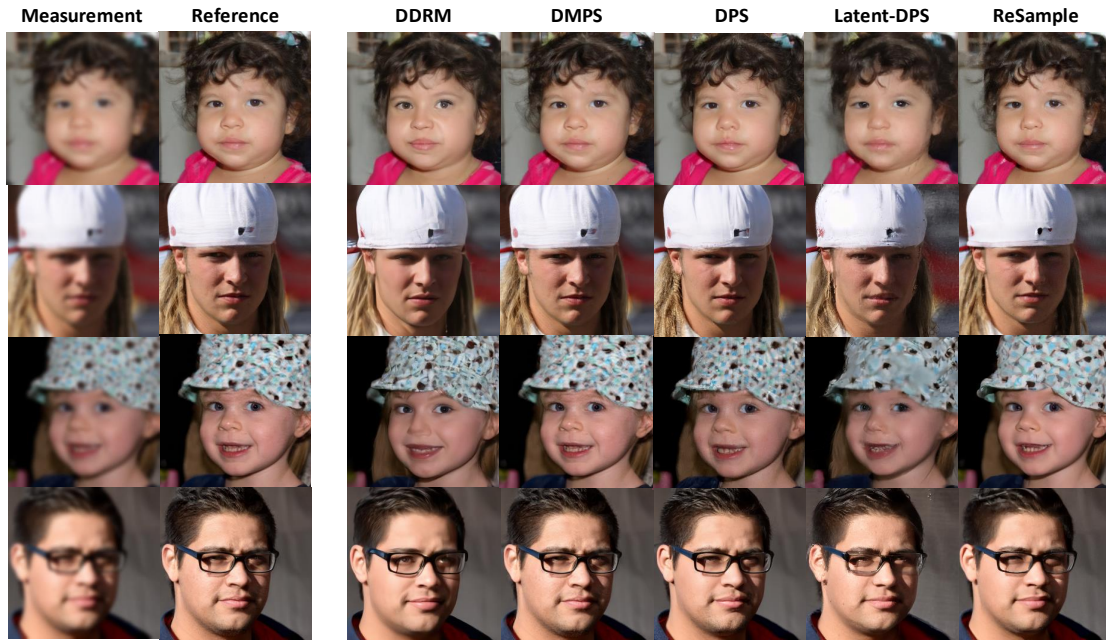


Figure 10: Comparison of algorithms on Gaussian deblurring on the FFHQ dataset with Gaussian measurement noise of variance $\sigma_y = 0.01$.

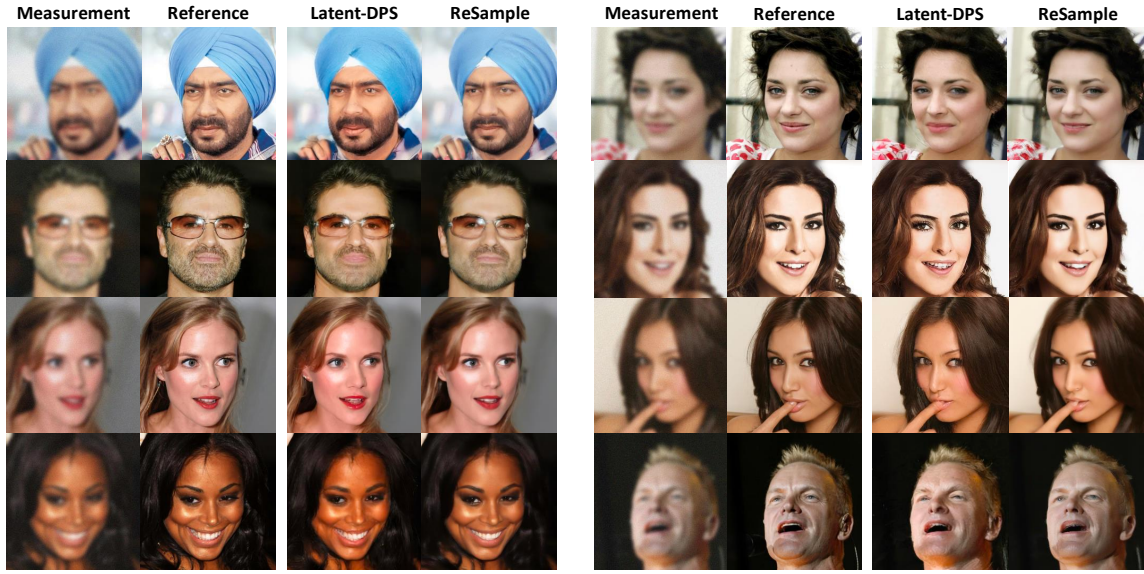


Figure 11: Additional results on Gaussian deblurring with additive Gaussian noise $\sigma_y = 0.05$.



Figure 12: Additional results on super resolution $4\times$ with additive Gaussian noise $\sigma_y = 0.05$.

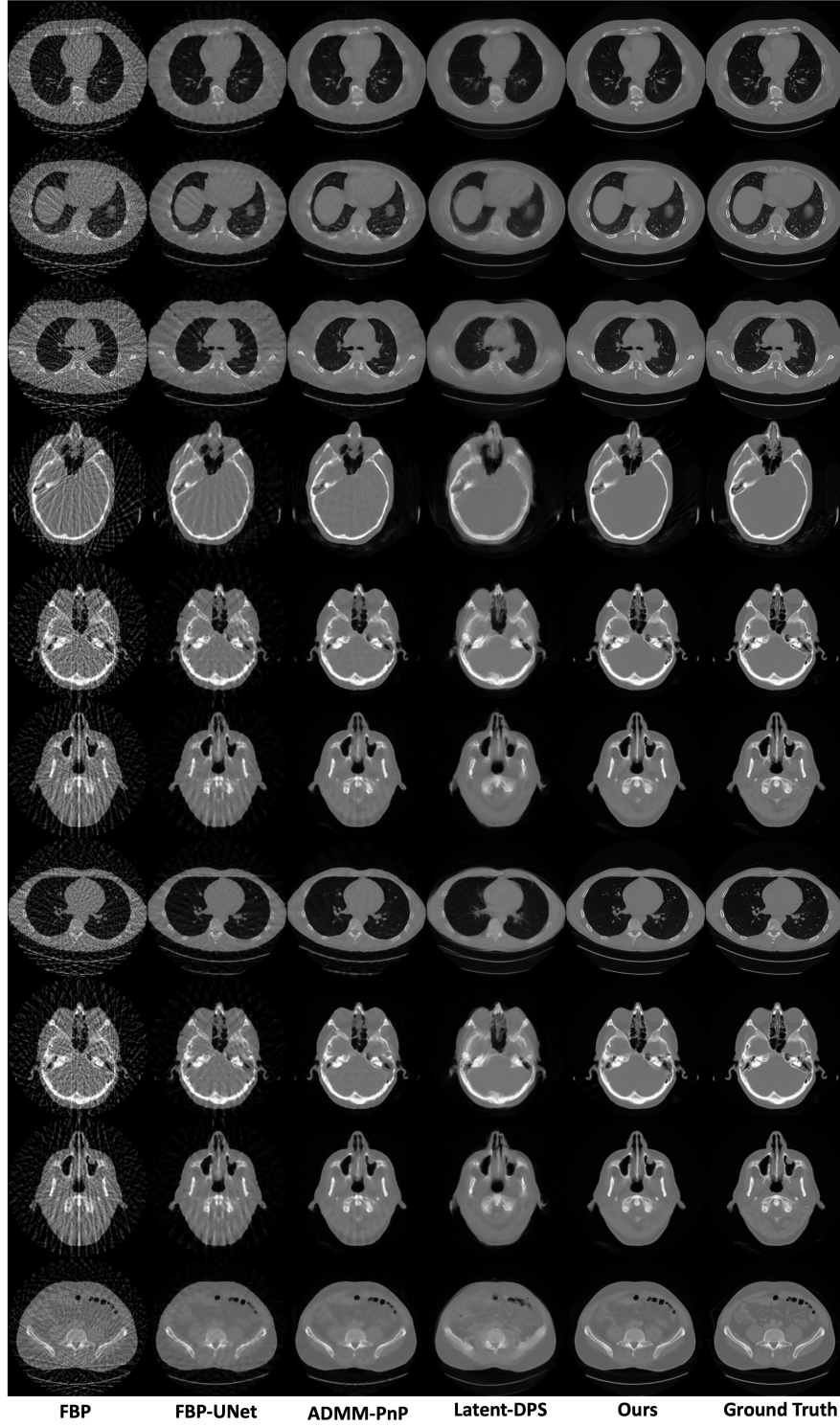


Figure 13: Additional results on CT reconstruction with additive Gaussian noise $\sigma_y = 0.01$.

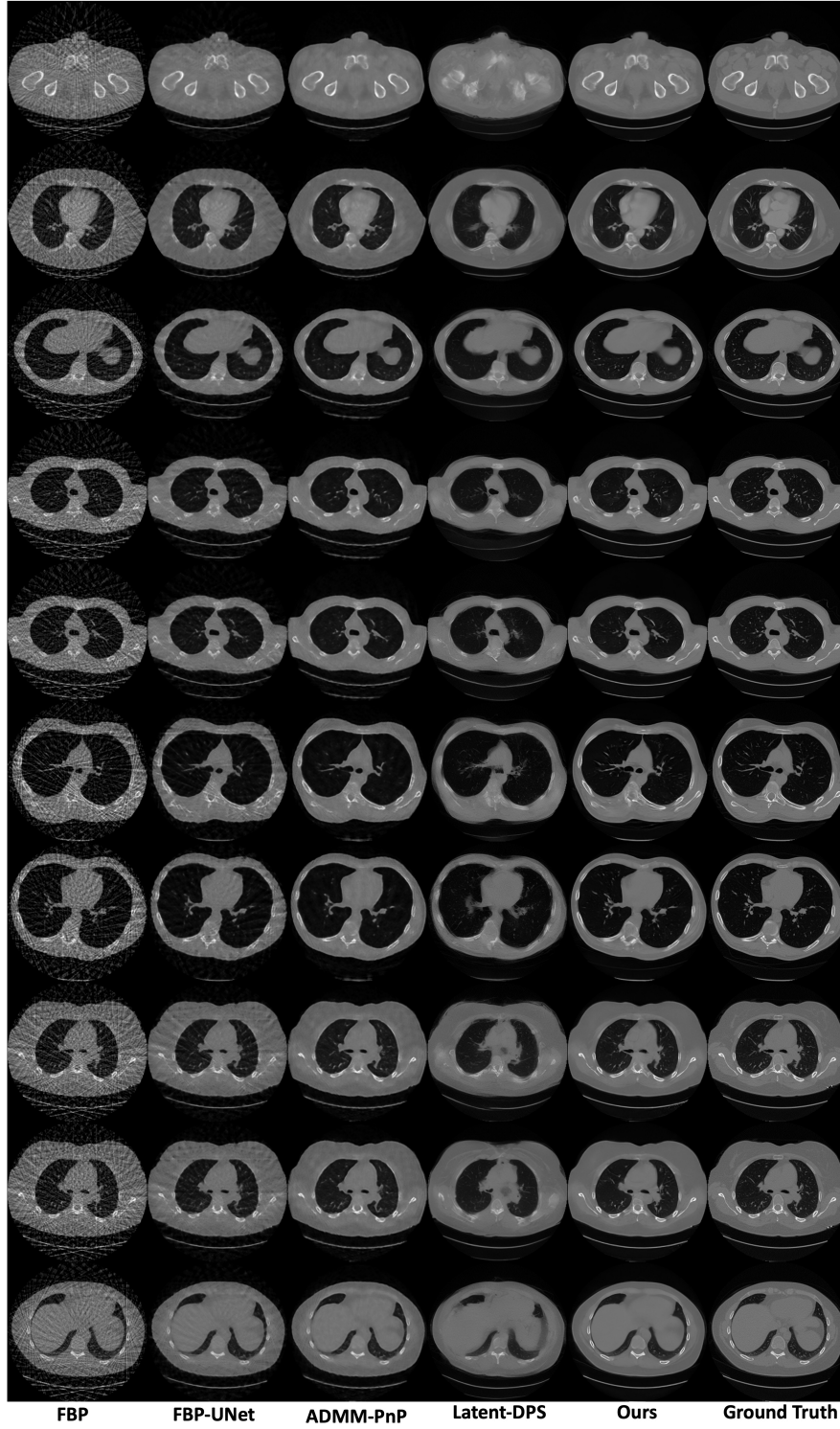


Figure 14: Additional results on CT reconstruction with additive Gaussian noise $\sigma_y = 0.01$.

A.3. Ablation Studies

Here, we present some ablation studies regarding computational efficiency and stochastic resampling, amongst others.

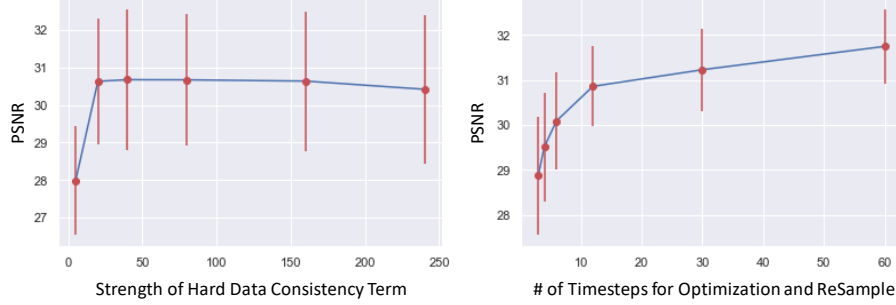


Figure 15: An ablation study on a few of the hyperparameters associated with ReSample. Left: Performance of different values of γ (hyperparameter in stochastic resampling) on the CelebA-HQ dataset. Right: CT reconstruction performance as a function of the number of timesteps to perform optimization.

Effectiveness of Stochastic Resampling. Recall that in stochastic resampling, we have one hyperparameter σ_t^2 . In Section C, we discuss that our choice for this hyperparameter is

$$\sigma_t^2 = \gamma \left(\frac{1 - \bar{\alpha}_{t-1}}{\bar{\alpha}_t} \right) \left(1 - \frac{\bar{\alpha}_t}{\bar{\alpha}_{t-1}} \right),$$

where $\bar{\alpha}$ is an adaptive parameter associated to the diffusion model process. Thus, the only parameter that we need to choose here is γ . To this end, we perform a study on how γ affects the image reconstruction quality. The γ term can be interpreted as a parameter that balances the prior consistency with the measurement consistency. In Figure 15 (left) observe that performance increases a lot when γ increases from a small value, but plateaus afterwards. We also observe that the larger γ gives more fine details on the images, but may introduce additional noise. In Figure 16, we provide visual representations corresponding to the choices of γ in order.

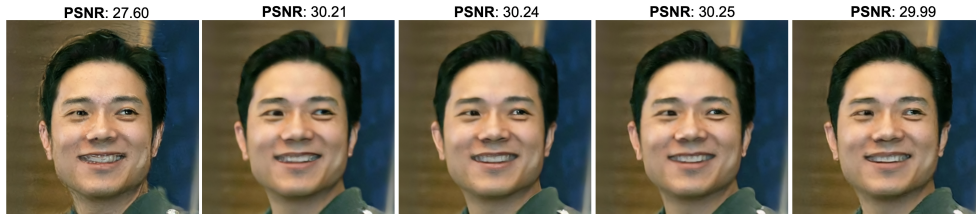


Figure 16: Visual representation of varying γ on the CelebA-HQ dataset.

Computational Efficiency. Here, we present the memory usage and inference times of ReSample compared to our baselines in Tables 7 and 8. We observe that the memory gap between ReSample and other algorithms widens when the pre-trained diffusion model increases in size, as the hard data consistency step of ReSample requires minimal memory. Conversely, since we only apply hard data consistency in a subset of all sampling steps (which differs from existing methods that

Table 7: Average inference of different algorithms for Gaussian Deblurring

Algorithm	Inference Time
DPS	1:12
MCG	1:20
DMPs	1:25
DDRM	10 seconds
PSLD	2:11
ReSample (Ours)	1:54

perform consistency updates at every time step), we note a slight increase in inference time compared to algorithms such as DPS, DMPS, and MCG. ReSample outperforms PSLD in terms of inference time.

Discussion on Latent-DPS. In the main text, we briefly discussed how adding the Latent-DPS gradient term into our ReSample algorithm *can* improve the overall reconstruction quality. Generally, we observe that adding the Latent-DPS gradient will cause a very marginal boost in the PSNR, but only when the learning rate scale is chosen “correctly”. Interestingly, we observe that choosing $\bar{\alpha}_t$ is *critical* in the performance of Latent-DPS. To this

end, we perform a brief ablation study on the learning rate for Latent-DPS, where we choose the learning rate to be $k\bar{\alpha}_t$ for some $k > 0$. We vary k and test the performance on 50 images of chest CT images and display the results in Table 9. In Table 9, we observe that $k = 0.5$ returns the best results, and should be chosen if one were to adopt the method of adding Latent-DPS into ReSample.

k	0	0.5	1.0	1.5	2.0	2.5
PSNR	31.64	31.73	31.58	31.51	31.27	31.04
Measurement Loss	9.82e-5	1.21e-4	5.03e-4	1.35e-3	1.96e-3	2.63e-3

Table 9: The effect of the Latent-DPS gradient scale (learning rate) as a function of $k > 0$. We study the PSNR and measurement loss (objective function) changes for varying k for chest CT reconstruction on 50 test samples. The best results are in bold. **NOTE:** $k = 0$ here refers to no Latent-DPS and only using ReSample.

Table 8: Memory Usage of different algorithms with different pretrained models for Gaussian Deblurring on FFHQ256 and ImageNet512 datasets

Pretrained Model	Algorithm	Model Only	Memory Increment	Total Memory
DDPM(FFHQ)	DPS	1953MB	+3416MB (175%)	5369MB
	MCG		+3421MB (175%)	5374MB
	DMPS		+5215MB (267 %)	7168MB
	DDRM		+18833MB (964 %)	20786MB
LDM(FFHQ)	PSLD	3969MB	+5516MB (140%)	9485MB
	ReSample (Ours)		+1040MB (26.2%)	5009MB
DDPM(ImageNet)	DPS	4394MB	+6637MB (151%)	11031MB
	MCG		+6637MB (151%)	11031MB
	DMPS		+8731MB (199 %)	13125MB
	DDRM		+4530MB (103 %)	8924MB
LDM(ImageNet)	PSLD	5669MB	+5943MB (105%)	11612MB
	ReSample (Ours)		+1322MB (30.1%)	7002MB

B. Discussion on Hard Data Consistency

Recall that the hard data consistency step involves solving the following optimization problem:

$$\hat{z}_0(\mathbf{y}) \in \arg \min_z \frac{1}{2} \|\mathbf{y} - \mathcal{A}(\mathcal{D}(z))\|_2^2, \quad (14)$$

where we initialize using $\hat{z}_0(z_t)$. Instead of solving for the latent variable z directly, notice that one possible technique would be to instead solve for vanilla least squares

$$\hat{x}_0(\mathbf{y}) \in \arg \min_x \frac{1}{2} \|\mathbf{y} - \mathcal{A}(x)\|_2^2, \quad (15)$$

where we instead initialize using $\mathcal{E}(\hat{z}_0(z_t))$, where $\mathcal{E}(\cdot)$ denotes the encoder. Throughout the rest of the Appendix, we refer to the former optimization process as *latent optimization* and the latter as *pixel optimization*. In our experiments, we actually found that these two different formulations yield different results, in the sense that performing latent optimization gives reconstructions that are “noisy”, yet much sharper with fine details, whereas pixel optimization gives results that are “smoother” yet blurry with high-level semantic information. Here, the intuition is that pixel optimization does not directly change the latent variable where as latent optimization directly optimizes over the latent variable. Moreover, the encoder $\mathcal{E}(\cdot)$ can add additional errors to the estimated $\hat{z}_0(\mathbf{y})$, perhaps throwing the sample off the data manifold, yielding images that are blurry as a result.

There is also a significant difference in time complexity between these two methods. Since latent optimization needs to backpropagate through the whole network of the decoder $\mathcal{D}(\cdot)$ on every gradient step, it takes much longer to obtain a local minimum (or converge). Empirically, to balance the trade-off between reconstruction speed and image quality, we see that using *both* of these formulations for hard data consistency can not only yield the best results, but also speed up the optimization process. Since pixel optimization is easy to get a global optimum, we use it first during the reverse sampling process and then use latent optimization when we are closer to $t = 0$ to refine the images with the finer details. We provide a depiction of this process in Figure 17.

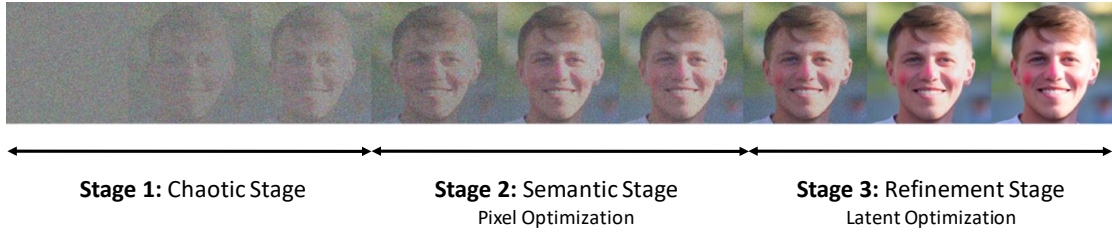


Figure 17: Depiction of the three stage process. During the second stage, we perform pixel optimization and latent optimization on the third stage for specific time steps t .

B.1. Accelerated Pixel Optimization by Conjugate Gradient

Notice that since pixel optimization directly operates in the pixel space, we can use solvers such as conjugate gradients least squares for linear inverse problems. Let \mathbf{A} be the matrix form of the linear operator $\mathcal{A}(\cdot)$. Then, the solution to the optimization problem is given by

$$\hat{x} = x_0 - \kappa(\mathbf{A}^+ \mathbf{A} x_0 - \mathbf{A}^+ \mathbf{y}), \quad (16)$$

where $\mathbf{A}^+ = \mathbf{A}^\top (\mathbf{A} \mathbf{A}^\top)^{-1}$ and $(\mathbf{A} \mathbf{A}^\top)^{-1}$ is implemented by conjugate gradients. κ is the hyperparameter that can be viewed as learning rate and x_0 is the initial (or prior) image before optimization, for which we use $\hat{x}_0(x_t)$.

We use this technique for CT reconstruction, where the forward operator \mathbf{A} is the radon transform and \mathbf{A}^\top is the non-filtered back projection. However, we can use this conjugate gradient technique for any linear inverse problem where the matrix \mathbf{A} is available.

C. Implementation Details

In this section, we discuss the choices of the hyperparameters used in all of our experiments for our algorithm. All experiments are implemented in PyTorch on NVIDIA GPUs (A100 and A40).

Notation	Definition
τ	Hyperparameter for early stopping in hard data consistency
σ_t	Variance scheduling for the resampling technique
T	Number of DDIM or DDPM steps

Table 10: Summary of the hyperparameters with their respective notations for ReSample.

C.1. Linear and Nonlinear Inverse Problems on Natural Images

For organizational purposes, we tabulate all of the hyperparameters associated to ReSample in Table 10. The parameter for the number of times to perform hard data consistency is not included in the table, as we did not have any explicit notation for it. For experiments across all natural images datasets (LSUN-Bedroom, FFHQ, CelebA-HQ), we used the same hyperparameters as they seemed to all empirically give the best results.

For T , we used $T = 500$ DDIM steps. For hard data consistency, we first split T into three even sub-intervals. The first stage refers to the sub-interval closest to $t = T$ and the third stage refers to the interval closest to $t = 0$. During the second stage, we performed pixel optimization, whereas in the third stage we performed latent optimization for hard data consistency as described in Section B. We performed this optimization on every 10 iterations of t .

We set $\tau = 10^{-4}$, which seemed to give us the best results for noisy inverse problems, with a maximum number of iterations of 2000 for pixel optimization and 500 for latent optimization (whichever convergence criteria came first). For the variance hyperparameter σ_t in the stochastic resample step, we chose an adaptive schedule of

$$\sigma_t^2 = \gamma \left(\frac{1 - \bar{\alpha}_{t-1}}{\bar{\alpha}_t} \right) \left(1 - \frac{\bar{\alpha}_t}{\bar{\alpha}_{t-1}} \right),$$

as discussed in Section A. Generally, we see that $\gamma = 40$ returns the best results for experiments on natural images.

C.2. Linear Inverse Problems on Medical Images

Since the LDMs for medical images is not as readily available as compared to natural images, we largely had to fine-tune existing models. We discuss these in more detail in this section.

Backbone Models. For the backbone latent diffusion model, we use the pre-trained model from latent diffusion [19]. We select the VQ-4 autoencoder and the FFHQ-LDM with CelebA-LDM as our backbone LDM. For inferencing, upon taking pre-trained checkpoints provided by [19], we fine-tuned the models on 2000 CT images with 100K iterations and a learning rate of 10^{-5} .

Inferencing. For T , we used a total of $T = 1000$ DDIM steps. For hard data consistency, we split T into three sub-intervals: $t > 750$, $300 < t \leq 750$, and $t \leq 300$. During the second stage, we performed pixel optimization by using conjugate gradients as discussed previously, with 50 iterations with $\kappa = 0.9$. In the third stage, we performed latent optimization with τ as the estimated noise level $\tau = 10^{-5}$ and $\lambda = 0$. We set skip step size to be 10 and $\gamma = 40$, with σ_t as the same as the experiments for the natural images.

C.3. Implementations of Baselines

Latent-DPS. For the Latent-DPS baseline, we use $T = 1000$ DDIM steps for CT reconstruction and $T = 500$ DDIM steps for natural image experiments. Let ζ_t denote the learning rate. For medical images, we use $\zeta_t = 2.5\bar{\alpha}_t$ and $\zeta_t = 0.5\bar{\alpha}_t$ for natural images. Empirically, we observe that our proposed ζ_t step size schedule gives the best performance and is robust to scale change, as previously discussed.

DPS and MCG. For DPS, we use the original DPS codebase provided by [11] and pre-trained models trained on CelebA and FFHQ training sets for natural images. For medical images, we use the pretrained checkpoint from [12] on the dataset provided by [35]. For MCG [12], we modified the MCG codebase by deleting the projection term tuning the gradient term for running DPS experiments on CT reconstruction. Otherwise, we directly used the codes provided by [12] for both natural and medical image experiments.

DDRM. For DDRM, we follow the original code provided by [13] with DDPM models trained on FFHQ and CelebA training sets adopted from the repository provided by [7]. We use the default parameters as displayed by [13].

DMPS. We follow the original code from the repository of [16] with the DDPM models trained on FFHQ and CelebA training sets adopted from the repository of [7]. We use the default parameters as displayed by [16].

PSLD. We follow the original code from the repo [37] with the pretrained LDMs on CelebA and FFHQ datasets provided by [19]. We use the default hyperparameters as implied in [37].

ADMM-PnP and Other (Supervised) Baselines. For ADMM-PnP we use the 10 iterations with τ tuned for different inverse problems. We use $\tau = 5$ for CT reconstruction, $\tau = 0.1$ for linear inverse problems, and $\tau = 0.075$ for nonlinear deblurring. We use the pre-trained model from original DnCNN repository provided by [38]. For FBP-UNet, we trained a UNet that maps FBP images to ground truth images. The UNet network architecture is the same as the one explained by [34].

D. More Discussion on the Failure Cases of Latent-DPS

In this section, we provide a further explanation to which why Latent-DPS often fails to give accurate reconstructions.

D.1. Failure of Linear Manifold Assumption

We hypothesize that one reason that Latent-DPS fails to give accurate reconstructions could be due to the nonlinearity of the decoder $\mathcal{D}(\cdot)$. More specifically, the derivation of DPS provided by [11] relies on a *linear manifold assumption*. For our case, since our forward model can be viewed as the form $\mathcal{A}(\mathcal{D}(\cdot))$, where the decoder $\mathcal{D}(\cdot)$ is a highly nonlinear neural network, this linear manifold assumption fails to hold. For example, if two images $\mathbf{z}^{(1)}$ and $\mathbf{z}^{(2)}$ lie on the clean data distribution manifold \mathcal{M} at $t = 0$, a linear combination of them $a\mathbf{z}^{(1)} + b\mathbf{z}^{(2)}$ for some constants a and b , may not belong to \mathcal{M} since $\mathcal{D}(a\mathbf{z}^{(1)} + b\mathbf{z}^{(2)})$ may not give us an image that is realistic. Thus, in practice, we observe that DPS reconstructions tend to be more blurry, which implies that the reverse sampling path falls out of this data manifold. We demonstrate this in Figure 18, where we show that the average of two latent vectors gives a blurry and unrealistic image.

We would like to point out that this reasoning may also explain why our algorithm outperforms DPS on nonlinear inverse tasks.

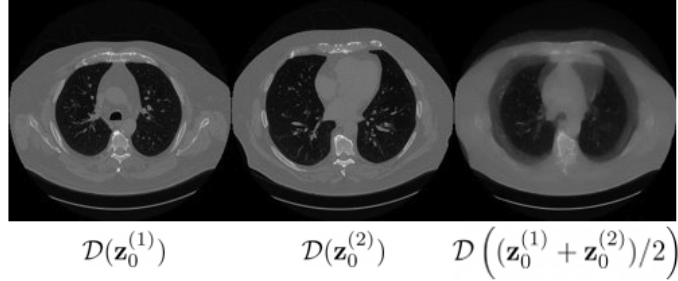


Figure 18: Depiction of the violation of the linear manifold assumption.

D.2. Inaccurate Estimates of the Posterior Mean

In this section, we discuss how inaccurate estimates of $\hat{\mathbf{z}}_0(\mathbf{z}_t)$ (i.e., the posterior mean via Tweedie’s formula) can be one of the reasons why Latent-DPS returns image reconstructions that are noisy. This was mainly because for values of t closer to $t = T$, the estimate of $\hat{\mathbf{z}}_0(\mathbf{z}_t)$ may be inaccurate, leading us to images that are noisy at $t = 0$. Generally, we find that the estimation of $\hat{\mathbf{z}}_0(\mathbf{z}_t)$ is inaccurate in the early timesteps (e.g. $t > 0.5T$) and vary a lot when t decreases. This implies that the gradient update may not point to a consistent direction when t is large. We further demonstrate this observation in Figure 19.

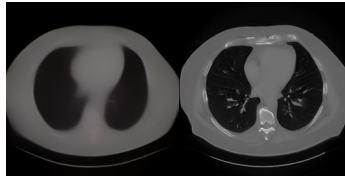


Figure 19: Comparison of the prediction of the ground truth signal $\hat{\mathbf{z}}_0(\mathbf{z}_t)$ for different values of t . Left: $\hat{\mathbf{z}}_0(\mathbf{z}_t)$ when $t = 0.5T$. Right: $\hat{\mathbf{z}}_0(\mathbf{z}_t)$ when $t = 0$. This serves to show the estimation error of the posterior mean for large values of t (i.e. when t is closer to pure noise).

E. Deferred Proofs for ReSample

Here, we provide the proofs regarding the theory behind our resampling technique. To make this section self-contained, we first restate all of our results and discuss notation that will be used throughout this section.

Notation. We denote scalars with under-case letters (e.g. α) and vectors with bold under-case letters (e.g. \mathbf{x}). Recall that in the main body of the paper, $\mathbf{z} \in \mathbb{R}^k$ denotes a sample in the latent space, \mathbf{z}'_t denotes an unconditional sample at time step t , $\hat{\mathbf{z}}_0(\mathbf{z}_t)$ denotes a prediction of the ground truth signal \mathbf{z}_0 at time step t , $\hat{\mathbf{z}}_0(\mathbf{y})$ denotes the measurement-consistent sample of $\hat{\mathbf{z}}_0(\mathbf{z}_t)$ using hard data consistency, and $\hat{\mathbf{z}}_t$ denotes the re-mapped sample from $\hat{\mathbf{z}}_0(\mathbf{y})$ onto the data manifold at time step t . We use $\hat{\mathbf{z}}_t$ as the next sample to resume the reverse diffusion process.

Proposition 1 (Stochastic Encoding). Since the sample $\hat{\mathbf{z}}_t$ given $\hat{\mathbf{z}}_0(\mathbf{y})$ and measurement \mathbf{y} is conditionally independent of \mathbf{y} , we have that

$$p(\hat{\mathbf{z}}_t|\hat{\mathbf{z}}_0(\mathbf{y}), \mathbf{y}) = p(\hat{\mathbf{z}}_t|\hat{\mathbf{z}}_0(\mathbf{y})) = \mathcal{N}(\sqrt{\bar{\alpha}_t}\hat{\mathbf{z}}_0(\mathbf{y}), (1 - \bar{\alpha}_t)\mathbf{I}). \quad (17)$$

Proof. By Tweedie's formula, we have that $\hat{\mathbf{z}}_0(\mathbf{y})$ is the estimated mean of the ground truth signal \mathbf{z}_0 . By the forward process of the DDPM formulation [22], we also have that

$$p(\hat{\mathbf{z}}_t|\hat{\mathbf{z}}_0(\mathbf{y})) = \mathcal{N}(\sqrt{\bar{\alpha}_t}\hat{\mathbf{z}}_0(\mathbf{y}), (1 - \bar{\alpha}_t)\mathbf{I}).$$

Then, since \mathbf{y} is a measurement of \mathbf{z}_0 at $t = 0$, we have $p(\mathbf{y}|\hat{\mathbf{z}}_0(\mathbf{y}), \hat{\mathbf{z}}_t) = p(\mathbf{y}|\hat{\mathbf{z}}_0(\mathbf{y}))$. Finally, we get

$$p(\hat{\mathbf{z}}_t|\hat{\mathbf{z}}_0(\mathbf{y}), \mathbf{y}) = \frac{p(\mathbf{y}|\hat{\mathbf{z}}_t, \hat{\mathbf{z}}_0(\mathbf{y}))p(\hat{\mathbf{z}}_t|\hat{\mathbf{z}}_0(\mathbf{y}))p(\hat{\mathbf{z}}_0(\mathbf{y}))}{p(\mathbf{y}, \hat{\mathbf{z}}_0(\mathbf{y}))} \quad (18)$$

$$= \frac{p(\mathbf{y}, \hat{\mathbf{z}}_0(\mathbf{y}))p(\hat{\mathbf{z}}_t|\hat{\mathbf{z}}_0(\mathbf{y}))}{p(\mathbf{y}, \hat{\mathbf{z}}_0(\mathbf{y}))} \quad (19)$$

$$= p(\hat{\mathbf{z}}_t|\hat{\mathbf{z}}_0(\mathbf{y})). \quad (20)$$

□

Proposition 2 (Stochastic Resampling). Suppose that $p(\mathbf{z}'_t|\hat{\mathbf{z}}_t, \hat{\mathbf{z}}_0(\mathbf{y}), \mathbf{y})$ is normally distributed such that $p(\mathbf{z}'_t|\hat{\mathbf{z}}_t, \hat{\mathbf{z}}_0(\mathbf{y}), \mathbf{y}) = \mathcal{N}(\mu_t, \sigma_t^2)$. If we let $p(\hat{\mathbf{z}}_t|\hat{\mathbf{z}}_0(\mathbf{y}), \mathbf{y})$ be a prior for μ_t , then the posterior distribution $p(\hat{\mathbf{z}}_t|\mathbf{z}'_t, \hat{\mathbf{z}}_0(\mathbf{y}), \mathbf{y})$ is given by

$$p(\hat{\mathbf{z}}_t|\mathbf{z}'_t, \hat{\mathbf{z}}_0(\mathbf{y}), \mathbf{y}) = \mathcal{N}\left(\frac{\sigma_t^2\sqrt{\bar{\alpha}_t}\hat{\mathbf{z}}_0(\mathbf{y}) + (1 - \bar{\alpha}_t)\mathbf{z}'_t}{\sigma_t^2 + (1 - \bar{\alpha}_t)}, \frac{\sigma_t^2(1 - \bar{\alpha}_t)}{\sigma_t^2 + (1 - \bar{\alpha}_t)}\mathbf{I}\right). \quad (21)$$

Proof. We have that

$$p(\hat{\mathbf{z}}_t|\mathbf{z}'_t, \hat{\mathbf{z}}_0(\mathbf{y}), \mathbf{y}) = \frac{p(\mathbf{z}'_t|\hat{\mathbf{z}}_t, \hat{\mathbf{z}}_0(\mathbf{y}), \mathbf{y})p(\hat{\mathbf{z}}_t|\hat{\mathbf{z}}_0(\mathbf{y}), \mathbf{y})p(\hat{\mathbf{z}}_0(\mathbf{y}), \mathbf{y})}{p(\mathbf{z}'_t, \hat{\mathbf{z}}_0(\mathbf{y}), \mathbf{y})}, \quad (22)$$

where both $p(\mathbf{z}'_t, \hat{\mathbf{z}}_0(\mathbf{y}), \mathbf{y})$ and $p(\hat{\mathbf{z}}_0(\mathbf{y}), \mathbf{y})$ are normalizing constants. Then by Lemma 1, we have $p(\hat{\mathbf{z}}_t|\hat{\mathbf{z}}_0(\mathbf{y}), \mathbf{y}) = \mathcal{N}(\sqrt{\bar{\alpha}_t}\hat{\mathbf{z}}_0(\mathbf{y}), (1 - \bar{\alpha}_t)\mathbf{I})$. Now, we can compute the posterior distribution:

$$p(\hat{\mathbf{z}}_t = \mathbf{k}|\mathbf{z}'_t, \hat{\mathbf{z}}_0(\mathbf{y}), \mathbf{y}) \propto p(\mathbf{z}'_t|\hat{\mathbf{z}}_t = \mathbf{k}, \hat{\mathbf{z}}_0(\mathbf{y}), \mathbf{y})p(\hat{\mathbf{z}}_t = \mathbf{k}|\hat{\mathbf{z}}_0(\mathbf{y}), \mathbf{y}) \quad (23)$$

$$\propto \exp\left\{-\left(\frac{(\mathbf{k} - \mathbf{z}'_t)^2}{\sigma_t^2}\right) + \left(\frac{(\mathbf{k} - \sqrt{\bar{\alpha}_t}\hat{\mathbf{z}}_0(\mathbf{y}))^2}{1 - \bar{\alpha}_t}\right)\right\} \quad (24)$$

$$\propto \exp\left\{-\frac{\left(\mathbf{k} - \frac{(1 - \bar{\alpha}_t)\mathbf{z}'_t + \sqrt{\bar{\alpha}_t}\hat{\mathbf{z}}_0(\mathbf{y})}{\sigma_t^2 + (1 - \bar{\alpha}_t)}\right)^2}{\frac{1}{\sigma_t^2} + \frac{1}{1 - \bar{\alpha}_t}}\right\}. \quad (25)$$

This is a Gaussian distribution, which can be easily shown using moment-generating functions [39].

□

Theorem 1. If $\hat{z}_0(\mathbf{y})$ is measurement-consistent such that $\mathbf{y} = \mathcal{A}(\mathcal{D}(\hat{z}_0(\mathbf{y})))$, i.e. $\hat{z}_0 = \hat{z}_0(\mathbf{z}_t) = \hat{z}_0(\mathbf{y})$, then stochastic resample is unbiased such that $\mathbb{E}[\hat{z}_t|\mathbf{y}] = \mathbb{E}[\mathbf{z}'_t]$.

Proof. We have that $\mathbb{E}[\hat{z}_t|\mathbf{y}] = \mathbb{E}_{\mathbf{z}'_t}[\mathbb{E}_{\hat{z}_0(\mathbf{y})}[\mathbb{E}_{\hat{z}_t}[\hat{z}_t|\mathbf{z}'_t, \hat{z}_0(\mathbf{y}), \mathbf{y}]]]$.

Let $\gamma = \frac{\sigma_t^2}{\sigma_t^2 + 1 - \bar{\alpha}_t}$. By using Proposition 2, we have $\mathbb{E}[\hat{z}_t|\mathbf{y}] = \mathbb{E}_{\mathbf{z}'_t}[\mathbb{E}_{\hat{z}_0}[(\gamma\sqrt{\bar{\alpha}_t}\hat{z}_0 + (1-\gamma)\mathbf{z}'_t)|\hat{z}_0, \mathbf{z}'_t, \mathbf{y}]]$.

Since \hat{z}_0 is measurement-consistent such that $\mathbf{y} = \mathcal{A}(\mathcal{D}(\hat{z}_0(\mathbf{y})))$, let $k = 0$, we have

$$\hat{z}_0(\mathbf{y}) = \hat{z}_0 = \frac{1}{\sqrt{\bar{\alpha}_{t-k}}}(\mathbf{z}'_{t-k} - (1 - \bar{\alpha}_{t-k})\nabla \log p(\mathbf{z}'_{t-k})) \quad (26)$$

Then, we have that

$$\mathbb{E}[\hat{z}_t|\mathbf{y}] = \mathbb{E}_{\mathbf{z}'_t}[\mathbb{E}_{\hat{z}_0}[(\gamma\sqrt{\bar{\alpha}_t}\hat{z}_0 + (1-\gamma)\mathbf{z}'_t)|\hat{z}_0, \mathbf{z}'_t, \mathbf{y}]] \quad (27)$$

$$= \gamma\sqrt{\frac{\bar{\alpha}_t}{\bar{\alpha}_{t-k}}}\mathbb{E}_{\mathbf{z}'_t}[\mathbb{E}[\mathbf{z}'_{t-k} - (1 - \bar{\alpha}_{t-k})\nabla \log p(\mathbf{z}'_{t-k})|\mathbf{z}'_t]] + (1-\gamma)\mathbb{E}[\mathbf{z}'_t], \quad (28)$$

as both \mathbf{z}'_t and \mathbf{z}'_{t-k} are unconditional samples and independent of \mathbf{y} . Now, we have

$$\mathbb{E}_{\mathbf{z}'_t}[\mathbb{E}[\mathbf{z}'_{t-k} - (1 - \bar{\alpha}_{t-k})\nabla \log p(\mathbf{z}'_{t-k})|\mathbf{z}'_t]] = \mathbb{E}_{\mathbf{z}'_{t-k}}[\mathbf{z}'_{t-k} - (1 - \bar{\alpha}_{t-k})\nabla \log p(\mathbf{z}'_{t-k})] \quad (29)$$

Since \mathbf{z}'_{t-k} is the unconditional reverse sample of \mathbf{z}'_t , we have $\mathbb{E}[\mathbf{z}'_t] = \sqrt{\frac{\bar{\alpha}_t}{\bar{\alpha}_{t-k}}}\mathbb{E}[\mathbf{z}'_{t-k}]$, and then

$$\mathbb{E}_{\mathbf{z}'_{t-k}}[\nabla \log p(\mathbf{z}'_{t-k})] = \int \nabla \log p(\mathbf{z}'_{t-k})p(\mathbf{z}'_{t-k})d\mathbf{z}'_{t-k} \quad (30)$$

$$= \int \frac{p'(\mathbf{z}'_{t-k})}{p(\mathbf{z}'_{t-k})}p(\mathbf{z}'_{t-k})d\mathbf{z}'_{t-k} \quad (31)$$

$$= \frac{\partial(1)}{\partial \mathbf{z}'_{t-k}} = 0 \quad (32)$$

Finally, we have $\mathbb{E}[\hat{z}_t|\mathbf{y}] = \gamma\mathbb{E}[\mathbf{z}'_t] + (1-\gamma)\mathbb{E}[\mathbf{z}'_t] = \mathbb{E}[\mathbf{z}'_t]$. \square

Lemma 1. Let \tilde{z}_t and \hat{z}_t denote the stochastically encoded and resampled image of $\hat{z}_0(\mathbf{y})$, respectively. If $\text{VAR}(\mathbf{z}'_t) > 0$, then we have that $\text{VAR}(\hat{z}_t) < \text{VAR}(\tilde{z}_t)$.

Proof. Recall that \hat{z}_t and \tilde{z}_t are both normally distributed, with

$$\text{VAR}(\hat{z}_t) = 1 - \bar{\alpha}_t \quad (33)$$

$$\text{VAR}(\tilde{z}_t) = \frac{1}{\frac{1}{1-\bar{\alpha}_t} + \frac{1}{\sigma_t^2}} \quad (34)$$

$$= \frac{\sigma_t^2(1 - \bar{\alpha}_t)}{\sigma_t^2 + (1 - \bar{\alpha}_t)}. \quad (35)$$

For all $\sigma_t^2 \geq 0$, we have

$$\frac{\sigma_t^2(1 - \bar{\alpha}_t)}{\sigma_t^2 + (1 - \bar{\alpha}_t)} < 1 - \bar{\alpha}_t \quad (36)$$

$$\implies \text{VAR}(\hat{z}_t) < \text{VAR}(\tilde{z}_t). \quad (37)$$

\square

Theorem 2. Let \mathbf{z}_0 denote a sample from the data distribution and \mathbf{z}_t be a sample from the noisy perturbed distribution at time t . Given that the score function $\nabla_{\mathbf{z}_t} \log p_{\mathbf{z}_t}(\mathbf{z}_t)$ is bounded,

$$\text{Cov}(\mathbf{z}_0|\mathbf{z}_t) = \frac{(1 - \bar{\alpha}_t)^2}{\bar{\alpha}_t} \nabla_{\mathbf{z}_t}^2 \log p_{\mathbf{z}_t}(\mathbf{z}_t) + \frac{1 - \bar{\alpha}_t}{\bar{\alpha}_t} \mathbf{I},$$

where $\alpha_t \in (0, 1)$ is an decreasing sequence in t .

Proof. By the LDM forward process, we have

$$p(\mathbf{z}_t | \mathbf{z}_0) = \mathcal{N}(\sqrt{\bar{\alpha}_t}, 1 - \bar{\alpha}_t).$$

Consider the following variable: $\hat{\mathbf{z}}_t = \frac{\sqrt{\bar{\alpha}_t}}{1 - \bar{\alpha}_t} \mathbf{z}_t$, which is simply a scaled version of \mathbf{z}_t . Then, consider the distribution

$$p(\bar{\mathbf{z}}_t | \mathbf{z}_0) = \frac{1}{\left(2\pi \left(\frac{\bar{\alpha}_t}{1 - \bar{\alpha}_t}\right)\right)^{d/2}} \exp \left\{ -\frac{\|\bar{\mathbf{z}}_t - \frac{\bar{\alpha}_t}{1 - \bar{\alpha}_t} \mathbf{z}_0\|_2^2}{2 \left(\frac{\bar{\alpha}_t}{1 - \bar{\alpha}_t}\right)} \right\}.$$

Now, we want to separate the term only with $\bar{\mathbf{z}}_t$ and the term only with \mathbf{z}_0 for applying Tweedie's formula. Hence, let $p_0(\bar{\mathbf{z}}_t) = \frac{1}{(2\pi(\frac{\bar{\alpha}_t}{1 - \bar{\alpha}_t}))^{d/2}} \exp \left(-\frac{\|\bar{\mathbf{z}}_t\|^2}{2(\frac{\bar{\alpha}_t}{1 - \bar{\alpha}_t})} \right)$, we achieve

$$p(\bar{\mathbf{z}}_t | \mathbf{z}_0) = p_0(\bar{\mathbf{z}}_t) \exp \left\{ \bar{\mathbf{z}}_t^\top \mathbf{z}_0 - \frac{\bar{\alpha}_t}{2(1 - \bar{\alpha}_t)} \|\mathbf{z}_0\|^2 \right\},$$

which separates the distribution interaction term $\bar{\mathbf{z}}_t^\top \mathbf{z}_0$ from $\|\mathbf{z}_0\|^2$ term.

Let $\lambda(\bar{\mathbf{z}}_t) = \log p(\bar{\mathbf{z}}_t) - \log p_0(\bar{\mathbf{z}}_t)$. Then by Tweedie's formula, we have $\mathbb{E}[\mathbf{z}_0 | \bar{\mathbf{z}}_t] = \nabla \lambda(\bar{\mathbf{z}}_t)$ and $\text{Cov}(\mathbf{z}_0 | \bar{\mathbf{z}}_t) = \nabla^2 \lambda(\bar{\mathbf{z}}_t)$. Since $p_0(\bar{\mathbf{z}}_t)$ is a Gaussian distribution with mean at 0 and variance equal to $\frac{\bar{\alpha}_t}{1 - \bar{\alpha}_t}$, we obtain

$$\nabla \lambda(\bar{\mathbf{z}}_t) = \nabla \log p(\bar{\mathbf{z}}_t) + \frac{1 - \bar{\alpha}_t}{\bar{\alpha}_t} \bar{\mathbf{z}}_t.$$

We observe that since $\hat{\mathbf{z}}$ is a scaled version of \mathbf{z}_t , we can obtain the distribution of $\hat{\mathbf{z}}$ as

$$p(\bar{\mathbf{z}}_t) = \frac{1 - \bar{\alpha}_t}{\sqrt{\bar{\alpha}_t}} p \left(\frac{1 - \bar{\alpha}_t}{\sqrt{\bar{\alpha}_t}} \cdot \mathbf{z}_t \right).$$

Then, we can apply chain rule to first compute then gradient on \mathbf{z}_t , and then account for $\bar{\mathbf{z}}_t$. As a result we get

$$\nabla_{\bar{\mathbf{z}}_t} \log p(\bar{\mathbf{z}}_t) = \frac{1 - \bar{\alpha}_t}{\sqrt{\bar{\alpha}_t}} \nabla_{\mathbf{z}_t} \log p(\mathbf{z}_t)$$

and then

$$\nabla \lambda(\bar{\mathbf{z}}_t) = \mathbb{E}[\mathbf{z}_0 | \mathbf{z}_t] = \frac{1 - \bar{\alpha}_t}{\sqrt{\bar{\alpha}_t}} \nabla \log p(\mathbf{z}_t) + \frac{1}{\sqrt{\bar{\alpha}_t}} \mathbf{z}_t,$$

which is consistent with the score function of [11]. Afterwards, we take the gradient again with respect to the $\bar{\mathbf{z}}_t$, and apply the chain rule again, then we have

$$\nabla^2 \lambda(\bar{\mathbf{z}}_t) = \text{Cov}(\mathbf{z}_0 | \mathbf{z}_t) = \frac{(1 - \bar{\alpha}_t)^2}{\bar{\alpha}_t} \nabla^2 \log p(\mathbf{z}_t) + \frac{1 - \bar{\alpha}_t}{\bar{\alpha}_t} \mathbf{I}.$$

This gives the desired result. \square